

Uncertainty quantification and sensitivity analysis for computational FFR estimation in stable coronary artery disease

Fredrik E. Fossan · Jacob Sturdy ·
Lucas O. Müller · Andreas Strand ·
Anders T. Bråten · Arve Jørgensen ·
Rune Wiseth · Leif R. Hellevik

Received: Na / Accepted: Na

Abstract We present a framework for the estimation of the Fractional Flow Reserve index based on blood flow simulations that incorporate clinical imaging and patient-specific characteristics. The process of model design implies making choices in order to build a suitable mathematical model, e.g. simulating a 3D domain versus a 1D domain, modeling of peripheral resistances, determining the regions of interest, etc. Here we thoroughly evaluate the impact of such choices on FFR prediction accuracy by reduced-order models with respect to more complete models by means of uncertainty quantification and sensitivity analysis. Moreover, we assess the uncertainty of FFR predictions based on our framework with respect to input data, and further determine the most influential inputs with sensitivity analysis, aiming at increasing the clinical usability of predictions by providing information on the reliability of model output on a per case basis. Analysis is carried out for a population of 13 patients for which 24 invasive FFR measurements are available. Our analysis confirms previously observed sources of uncertainty and provides insight into aspects to be improved in any model-based non-invasive FFR estimation method.

Keywords computational FFR · uncertainty quantification · model complexity · total uncertainty

1 Introduction

Ischemic heart disease is the leading cause of death globally [33], and its relevance will increase as the global population ages. In this study we consider

Norwegian University of Science and Technology
NO-7491 Trondheim, Norway
Tel.: +123-45-678910
Fax: +123-45-678910
E-mail: fredrik.e.fossan@ntnu.no

patients with stable Coronary Artery Disease (CAD) which, in addition to acute myocardial infarction, is the main symptomatic manifestation of coronary artery disease. In this context, Fractional Flow Reserve (FFR) has been shown to be a reliable, but invasive, tool to study the functional significance of coronary artery stenosis. Further, FFR-guided revacularization has improved event-free survival and lower healthcare costs in randomized studies [49, 34, 7]. Over the last decade many attempts have been made to predict FFR non-invasively using computational fluid dynamics and mathematical models [6].

Seeking clinical applicability, many proposed methods for non-invasive FFR prediction rely on simplified versions of the original physical problem, i.e. simplifications to the original problem are made in order to reduce computational cost and to allow for a fast calculation of FFR, see for example [19, 35]. However, in such studies no information on the errors made by using simplified models are provided. Two notable exceptions are found in [3, 2], where results obtained using reduced, one-dimensional blood flow models are validated by comparison to results obtained using 3D transient models for a synthetically generated population and for a real patient population, respectively. However, in both cases the impact of modelling assumptions chosen to simplify the problem is either only partially explored or completely ignored. We perform an extensive evaluation of the impact of model reduction choices on FFR predictions by using uncertainty quantification and sensitivity analysis (UQ&SA) tools. These tools are extremely useful in addressing such questions, as UQ&SA provide insight into which elements of the simplified model are most influential on FFR prediction and are thus ideal candidates for optimization.

A few previous studies have investigated the sensitivity of FFR predictions to various sources of uncertainty in patient-specific models of coronary flow [41, 30], while others have analyzed generic models of coronary blood flow and stenoses as general investigations into the uncertainty of model predicted FFR [9, 48]. Sankaran et al. [41] and Morris et al. [30] both investigated the effects of uncertainty in computational prediction of FFR. Sankaran et al. accounted for uncertainties in lesion geometry, peripheral resistance and blood viscosity, while Morris et al. considered only uncertainty about parameters for a lumped stenosis model, proximal pressure, and resistance in the coronary microvasculature.

This study extends the above mentioned previous works by including uncertainties in additional parameters required for performing a computational assessment of FFR. Additionally, by performing such a study on a population of patient-specific cases, we provide further insight into the role played by different parameters for different ranges of FFR, with particular attention to intermediate stenoses with FFR values between 0.7 and 0.9, showing how the various sources of uncertainty may impact individual cases differently.

The noninvasive, sampling based UQ&SA methods of Monte-Carlo and Polynomial chaos are employed to estimate global Sobol sensitivity indices which assess sensitivity by partitioning the uncertainty in the model output into components associated with particular inputs. Further these methods approximate the distribution of the model output from which summary quan-

ties may be calculated to describe the resulting uncertainty in FFR model prediction where desired.

The rest of this paper is structured as follows. In Sect. 2 we introduce two predictive models of FFR based on 3D incompressible Navier-Stokes and reduced-order one-dimensional flow, respectively. Additionally we describe the the UQ&SA framework in Sect. 2. Next, in Sect. 3 we present results for the optimal reduced-order model setup, as well as for the UQ&SA analysis performed on FFR predictions. Finally, in Sect. 4 we discuss presented results as well as considerations on further steps to be taken in order to increase the accuracy and reduce the uncertainty in model-based FFR prediction.

2 Materials and methods

2.1 Study population

We consider a population of 13 patients that underwent invasive angiography and FFR measurement after clinical and coronary computed tomography angiography (CCTA) examinations indicated stable CAD. We collected 24 FFR measurements from these patients. The FFR measurements had a mean of 0.77 and a standard deviation of 0.17, with a positive FFR prevalence of 41.67 % for a cutoff value of $\text{FFR} < 0.8$. The patients were recruited as part of an ongoing clinical trial at St. Olavs Hospital, Trondheim, Norway [?].

2.1.1 Recruitment

The study subjects included in the analysis had undergone coronary computed tomography angiography (CCTA) due to chest pain and suspicion of stable CAD. Patients were enrolled with the findings of one or more coronary stenosis on CCTA and being further referred for invasive coronary angiography (ICA) with invasive FFR measurements.

Exclusion criteria included unstable coronary heart disease, previous percutaneous coronary intervention or bypass surgery, renal insufficiency (estimated glomerular filtration rate $< 30 \text{ mL/min}$), obesity ($\text{BMI} > 40$), non diagnostic quality of the CCTA due to motion artifacts or known allergy to contrast agent or contraindications to adenosine.

2.1.2 Data acquisition

CCTA was performed using two CT scanners with 2×128 detector rows (Siemens dual source Definition Flash) using a standardized protocol [14].

Echocardiographic imaging was performed using a GE Vivid E95 scanner (GE Vingmed Ultrasound, Horten, Norway). Cardiac output (CO) was calculated based on cross-sectional area of left ventricle outflow tract measured immediately proximal to the points of insertion of the aortic leaflets and velocity time integral derived from PW Doppler.

Fractional flow reserve was measured using Verrata Plus (Philips Volcano, San Diego, USA) pressure wires according to standard practice. Intra-coronary nitroglycerin (0.2 mg) was given to all patients before advancing the pressure wire into the coronary arteries and hyperemia was induced by continuous intravenous infusion of adenosine at a rate of at least 140 µg/kg/min. FFR measurements were taken during the nadir of the Pd/Pa tracings. After measurement the interventional cardiologist removed the pressure wire back to the equalization point at the tip of the guiding catheter, to ensure that there was no drift.

Blood pressure measurements (P_{meas}) were performed on both arms as part of clinical routine before ICA using an automatic, digital BP device, Welch Allyn ProBP 3400.

2.2 Estimation of FFR from CCTA images

2.2.1 Computational domain segmentation and meshing

Segmentation of vessels was performed using the open-source software ITK-SNAP [54], which provides a user-friendly interface for a semi-automatic active contour evolution approach. The output of ITK-SNAP is a labeled voxel volume identifying voxels labeled as vessels and a surface mesh of the segmented volume (in VTK format). Surface mesh processing, flow extensions addition and meshing were performed using the open-source library Vascular Modeling ToolKit (VMTK) [1, 47]. The meshing refinement level was determined by a meshing algorithm parameter called edge-length factor l_f , which was set to $l_f = 0.21$ for all simulations. A mesh independence study showed that such discretization provides mesh independent FFR predictions for a set of 4 patient-specific geometries.

2.2.2 3D modeling framework

Mathematical model. We consider the domain defined by the coronary tree vessels as $\Omega_f \in \mathbb{R}^3$. Moreover, its boundary is partitioned as $\partial\Omega_f := \Gamma_{\text{in}} \cup \Sigma \cup \Gamma_{\text{out}}$, where Σ represents the wall boundary, Γ_{in} is the inlet cross-section and $\Gamma_{\text{out}} = \bigcup_{j=1}^{N_{\text{out}}} \Gamma_{\text{out},j}$ is the union of the N_{out} outlets of the tree. Furthermore, blood flow in coronary arteries is modeled assuming that blood is an incompressible Newtonian fluid, for which the incompressible Navier-Stokes equations hold. These equations, along with boundary conditions are given by

$$\begin{cases} \frac{\partial \mathbf{u}}{\partial t} + \mathbf{u} \cdot \nabla \mathbf{u} = -\frac{1}{\rho} \nabla p + \nu \nabla^2 \mathbf{u} & \text{in } \Omega_f, \\ \nabla \cdot \mathbf{u} = 0 & \text{in } \Omega_f, \\ \mathbf{u} = \mathbf{0} & \text{on } \Sigma, \\ p = P_{\text{in}}(t) & \text{on } \Gamma_{\text{in}}, \text{ and} \\ p = P_{\text{out},j}(t) & \text{on } \Gamma_{\text{out},j}, \quad j = 1, 2, \dots, N_{\text{out}}, \end{cases} \quad (1)$$

where $P_{\text{in}}(t)$ is a prescribed pressure function and $P_{\text{out},j}(t)$ is provided by the lumped-parameter model that is coupled to the j -th outlet. In fact, each outlet is coupled to a lumped-parameter model [24], which in turns derives from the original work by Mantero et al. [28]. This lumped-parameter model setup is depicted in Fig. 1 and is governed by the ordinary differential equations (ODEs)

$$\begin{cases} \frac{dV_{\text{ca}}}{dt} = Q_{\text{out}} - Q_{\text{m}}, \\ \frac{dV_{\text{m}}}{dt} = Q_{\text{m}} - Q_{\text{d}}. \end{cases} \quad (2)$$

Volumes relate to pressure at corresponding compartments by

$$\begin{cases} P_{\text{ca}} = \frac{V_{\text{ca}}}{C_{\text{ca}}}, \\ P_{\text{cm}} = \frac{V_{\text{cm}}}{C_{\text{cm}}} + P_{\text{LV}}, \end{cases} \quad (3)$$

where P_{LV} is the left ventricular pressure.

Flow $Q_{\text{out},j}$, for the j -th outlet, is computed as

$$Q_{\text{out},j} = \int_{\Gamma_{\text{out},j}} \mathbf{u} \cdot \mathbf{n}_{\text{out},j} dS, \quad (4)$$

where $\mathbf{n}_{\text{out},j}$ is the exterior unit-vector normal for $\Gamma_{\text{out},j}$. On the other hand, $P_{\text{out},j}$ is provided by the lumped-parameter model as

$$P_{\text{out},j} = \text{MAP}_j + R_{\text{p},j} Q_{\text{out},j}. \quad (5)$$

Numerical methods. The mathematical models presented in Section 2.2.2 are solved using the open-source library CBCFLOW [11], based on FEniCS [27]. In particular, CBCFLOW provides a flexible problem setup, allowing to combine its highly efficient incompressible Navier-Stokes solver with typical boundary conditions and simple models used in computational hemodynamics. Here, a python script allowed CBCFLOW to interact with lumped-parameter models and to prescribe the needed boundary conditions.

The problem defined by Eq. (1) is solved by CBCFLOW using the Incremental Pressure Correction Scheme, described in [44]. The solver implementation follows very closely the one reported in [31]. Apart from spatial

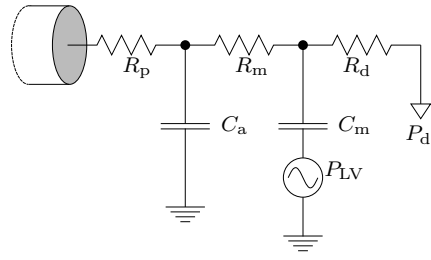


Fig. 1: Schematic representation of a lumped-parameter model coupled to a 3D domain outlet Γ_j^{out} and related to Eq. (2) and Eq. (3). Portion of the 3D domain is also shown.

and temporal discretization, the only numerical parameter to be set for this scheme is a multiplicative factor for the streamline diffusion stabilization term, referred to as s in this work, see [55] for details about this term. Moreover, Eqs. (2) are solved using an explicit Euler discretization. Numerical parameters are set to $\Delta t = 1 \text{ ms}$ and $s = 1$. A parameter independence study has shown that such choices provide parameter independent FFR predictions for a set of patient-specific geometries.

Definition of main parameters from patient-specific data. For each patient, the following patient-specific data is used:

- proximal and distal pressure tracings acquired during invasive FFR measurement for baseline and hyperemic conditions,
- cardiac output derived from ultrasonographic examination,
- computational domain extracted from CCTA data.

The following paragraphs describe the process of personalizing the model to patient-specific details. The flow to the coronary branch is based on the work of Sakamoto et al. [38], who studied the dependence of flow on coronary branch dominance. From this we calculate the relative distribution of total coronary flow, γ_k^j , to each coronary branch j for people with k dominant vasculature ($j = \{\text{RCA}, \text{LM}\}$ and $k = \{\text{LeftDom}, \text{RightDom}\}$). Furthermore, total coronary flow was assumed to be 4.5 % of CO. Thus, the baseline coronary flow to the left or right branch is

$$q_{\text{cor}}^j = 0.045 \cdot \gamma_k^j \cdot \text{CO}. \quad (6)$$

The two flow fractions may be combined to get the fraction of CO to a branch, $\lambda_{\text{cor}} = 0.045 \cdot \gamma_k^j$. Total peripheral compliance is computed as a percentage of total arterial compliance of 1.7 mL mmHg^{-1} . The percentage of the total arterial compliance assigned to the left/right branch is equal to the relation between flow in branch of interest over total cardiac output, that is

$$C_{\text{tot}} = q_{\text{cor}}^j / \text{CO} \times 1.7 \text{ mL mmHg}^{-1}. \quad (7)$$

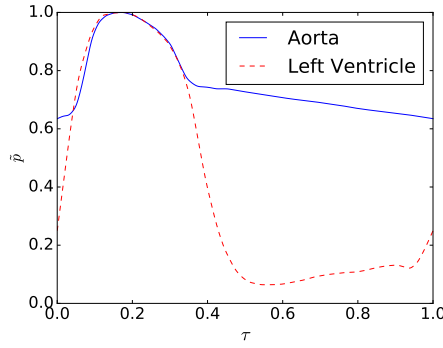


Fig. 2: Aortic and left ventricle characteristic waveforms used for patient-specific simulations. τ and \tilde{p} are normalized time and pressure. The waveform shapes were taken from [24].

Mean Arterial Pressure (MAP) and Pulse Pressure (PP) are extracted from pressure tracings, as well as cardiac cycle duration T . MAP and PP are used to prescribe a scaled characteristic aortic pressure waveform at the network's inlet and a scaled characteristic left ventricle pressure waveform (peak left ventricle pressure is 1.05 times the peak inlet pressure) for all lumped-parameter models. The characteristic waveforms are shown in Fig. 2. Total peripheral resistance is estimated from MAP and the target branch flow in baseline conditions q_{cor}^j as

$$R_{\text{tot}} = \frac{\text{MAP} - P_d}{q_{\text{cor}}^j}. \quad (8)$$

The total peripheral resistance R_{tot} and total peripheral compliance C_{tot} are distributed among outlets using Murray's law, that is

$$R_j = \frac{\sum_{i=1}^{N_{\text{out}}} r_i^3}{r_j^3} R_{\text{tot}} \quad (9)$$

and

$$C_j = \frac{r_j^3}{\sum_{i=1}^{N_{\text{out}}} r_i^3} C_{\text{tot}}, \quad (10)$$

where j stands for the j -th outlet of the network. R_j and C_j have to be subsequently distributed among the different compartments (see Figure 1) of the lumped-parameter model attached to the j -th outlet. The fractions for distributing R_j among $R_{p,j}$, $R_{m,j}$ and $R_{d,j}$ are set to 0.01, 0.84 and 0.15, respectively. Similarly, fractions used to distribute C_j among $C_{a,j}$ and $C_{m,j}$ are 0.025 and 0.975, respectively.

Modeling pipeline. The modeling pipeline is as follows

1. Using parameters defined in this section as initial guess, total peripheral resistance R_{tot} is modified in order to match target branch flow q_{cor} defined by Eq. (6). The iterative procedure is described later in this section.
2. We determine heart rate, MAP and PP from pressure tracings taken under hyperemic conditions. Moreover, we use R_{tot} from previous step to estimate a new total peripheral resistance, now in hyperemic conditions: $R_{\text{tot,hyp}} = R_{\text{tot}}/\alpha$, which is subsequently distributed among outlets with criteria specified in Eq. (9). The hyperemic factor, α , was set to 3.
3. Once the transient simulation is available, we compute equivalent total resistances for each outlet using the resulting cardiac cycle averaged outlet pressure and flow, and perform a simulation using the same numerical framework while prescribing MAP and total resistances, thus obtaining a simulation that approaches a steady state.

Solution monitoring and total resistance estimation. As noted previously, total peripheral resistance R_{tot} is modified in order to match average branch flow q_{cor} defined in Eq. (6). Starting with the initial guess provided by Eq. (8), R_{tot} is updated after each cardiac cycle using

$$R_{\text{tot}}^{m+1} = R_{\text{tot}}^m (1 - \omega(q_{\text{cor}} - q_{\text{obs}})/q_{\text{cor}}) , \quad (11)$$

where m is the iteration index (which corresponds to the cardiac cycle index), q_{cor} is the target coronary flow in a branch, provided by Eq. (6) and q_{obs} is the observed flow at the branch inlet. ω is a relaxation parameter and was set to $\omega = 0.9$. Once that a new value for R_{tot} is available, the resistance is distributed among outlets using Eq. (9).

In order to extract predicted FFR, we computed spatial averages for pressure over 3D subdomains defined as

$$\Omega_{f,k} := \{\mathbf{x} \in \Omega_f : \|\mathbf{x} - \mathbf{x}_k\| < r_k\} , \quad (12)$$

where \mathbf{x}_k is the k -th node of a vessel's centerline that corresponds to the point where the invasive FFR measurement was taken, and r_k is the radius of the vessel at node k . Locations \mathbf{x}_k were identified by inspection of angiograms and segmentation results by modelers and cardiologists.

2.3 Reduced order model

One-dimensional blood flow in elastic compliant vessels can be described in terms of pressure and flow (P, Q) by

$$\frac{\partial A}{\partial P} \frac{\partial P}{\partial t} + \frac{\partial Q}{\partial x} = 0, \quad (13a)$$

$$\frac{\partial Q}{\partial t} + \frac{\partial}{\partial x} \left(\frac{Q^2}{A} \right) = -\frac{A}{\rho} \frac{\partial P}{\partial x} + \frac{f}{\rho}, \quad (13b)$$

where $f = -2(\zeta + 2)\mu\pi U$ is the frictional term, ρ is the density, μ is the viscosity of blood, A is the cross-sectional area and U is the cross-sectional averaged velocity. The velocity profile is prescribed by

$$u(x, \xi, t) = U(x, t) \frac{\zeta + 2}{\zeta} \left[1 - \left(\frac{\xi}{r} \right)^\zeta \right], \quad (14)$$

where $r(x, t)$ is the lumen radius, ξ is the radial coordinate and ζ is the polynomial order.

At arterial connections, conservation of mass and a coupling relations are enforced, i.e.

$$\sum_{i=1}^N Q_i = 0, \quad (15a)$$

$$P_1 + \lambda \frac{\rho}{2} U_1^2 = P_i + \lambda \frac{\rho}{2} U_i^2 + \Delta P_i \quad i = 2, \dots, N, \quad (15b)$$

where N is the number of vessels in the connection, ΔP is an additional pressure loss and λ is a coefficient between zero and one. At healthy junctions, ΔP is set to zero and λ is set to one, so that Eq. (15b) describes continuity of total pressure. At arterial stenoses, the flow regimes are 3D and the 1D assumptions no longer hold. Stenotic regions are thus removed and treated as junctions with $N = 2$. Moreover, λ is set to zero, and ΔP is an experimentally derived pressure loss term given by [53]. Here we use an equivalent expression, reported in [26], namely

$$\Delta P = \frac{K_v \mu}{A_0 D_0} Q + \frac{K_t \rho}{2 A_0^2} \left(\frac{A_0}{A_s} - 1 \right)^2 Q |Q|, \quad (16)$$

where A_0 and A_s refer to cross-sectional areas of the normal and stenotic segments, respectively. Similarly, D_0 and D_s represent the normal and stenotic diameters, whereas L_s is the length of the stenosis. Furthermore, K_v and K_t are empirical coefficients, with $K_v = 32(0.83 L_s + 1.64 D_s) \cdot (A_0/A_s)^2 / D_0$ and $K_t = 1.52$ [26].

Eqs. (13a)-(13b) are commonly used to model pulse wave propagation in the cardiovascular system. A pressure-area relation is required in order to close the system, which for elastic vessel walls assumes the form of an algebraic relation. However, as we will show later, FFR predictions can be obtained by neglecting transient terms, thus we can use the steady state version of Eqs. (13a)-(13b), which, in terms of steady state variables \bar{P} and \bar{Q} , reads

$$\bar{Q}_{\text{in}} = \bar{Q}_{\text{out}}, \quad (17a)$$

$$\bar{P}_{\text{in}} + \frac{\rho}{2} \left(\frac{\bar{Q}_{\text{in}}}{\bar{A}_{\text{in}}} \right)^2 = \bar{P}_{\text{out}} + \frac{\rho}{2} \left(\frac{\bar{Q}_{\text{out}}}{\bar{A}_{\text{out}}} \right)^2 + \bar{Q}_{\text{in}} \int_0^l \frac{2(\zeta + 2)\pi\mu}{\bar{A}^2} dx, \quad (17b)$$

where l is the length of the 1D segment, X_{in} denotes variables at the inlet of the segment and X_{out} denotes variables at the outlet. As for the 3D case, steady state simulations are performed prescribing a constant pressure at the inlet of a given coronary network and resistances at its outlets.

Numerical solution Consider a network of D vessels with M outlets, at which terminal resistances $R_{\text{out},j}$, with $j = 1, 2, \dots, M$, are attached. The pressure distribution in this network is uniquely defined by setting outlet flows, $Q_{\text{out},j}$, with $j = 1, 2, \dots, M$. As previously stated, in our modeling framework we prescribe pressure at the inlet of the network. Finding the pressure distribution over the network for this setting reduces to solving a system of nonlinear algebraic equations for the M unknown outlet flows, i.e. $\mathbf{x} = [Q_{\text{out},1}, Q_{\text{out},2} \dots Q_{\text{out},M}]$. $M-1$ equations are given by coupling equations for the pressures at junctions, Eqs. (15b), and an additional equation is provided to enforce that the inlet boundary condition is fulfilled, i.e. $P_{\text{in}}^{\text{presc}} = \bar{P}_{\text{in},k}$, where k is the index of the inlet vessel of the network and $P_{\text{in}}^{\text{presc}}$ is the pressure to be prescribed. The solution \mathbf{x}^* thus satisfies $\mathbf{f}(\mathbf{x}^*) = \mathbf{0}$, where \mathbf{f} are the aforementioned (residual) equations. For a given \mathbf{x} , \mathbf{f} is evaluated by distributing the outlet flows along the coronary tree by ensuring conservation of mass according to Eq. (15a). Furthermore, the pressure at outlets are found from

$$P_{\text{out},j} = P_{\text{d}} + R_{\text{out},j} Q_{\text{out},j}, \quad (18)$$

where $P_{\text{d}} = 5 \text{ mmHg}$ is the outflow pressure. The pressure drop, $\Delta P_{1\text{D}-0\text{D}}$, from the inlet to the outlet of a 1D-0D segment, for a given flow Q , was calculated from Eqs. (16) and (17b), where the integral $\int_0^l \frac{2(\zeta+2)\pi\mu}{A^2} dx$ was estimated using the trapezoidal rule. For a junction with N vessels there are $N-1$ daughter (d) vessels and $N-1$ equations relating pressure and flows at a junction. We reserve one such equation in the evaluation of \mathbf{f} , to relate the pressure in the outlet of the mother vessel (m) for the given flows Q_m , Q_d and pressure P_d . (The remaining $N-2$ equations are used as residual equations in \mathbf{f} .) With this we can traverse from outlets to the inlet and assign flow in addition to inlet and outlet pressure in all 1D-0D segments, necessary to evaluate \mathbf{f} . The python based optimization tool `scipy.optimize.minimize.root` [22] was used to solve the nonlinear problem with a tolerance of 10^{-10} Pa . The solution procedure is summarized in Algorithm 1.

Algorithm 1 Numerical solution of 1D-0D model.

- 1: initial guess of \mathbf{x}
 - 2: $\text{tol} = 10^{-10}$
 - 3: **while** $\max(|\mathbf{f}|) \geq \text{tol}$ **do**
 - 4: distribute flow in network by enforcing Eq. (15a) at junctions
 - 5: calculate pressure in terminal segments $P_{\text{out},j}$ according to Eq. (18)
 - 6: calculate ΔP in all 1D-0D segment according to Eqs. (16) and (17b)
 - 7: traverse from outlet to inlet and distribute pressure in the network based on ΔP and coupling equations Eqs. (15b) at each junction
 - 8: evaluate \mathbf{f}
 - 9: update \mathbf{x}
-

2.3.1 From 3D domain to a 1D network

The construction of a network of 1D domains from the original 3D domain involves a series of non-trivial steps. Here we describe them in detail. The methods illustrated in this section are a modification of those proposed in [2]. All steps described here were performed using VMTK [1] and VTK [42] libraries via python scripting.

Skeletonization of the 3D domain. In order to obtain the 1D network, centerlines of the 3D volume meshes were generated and cross-sectional areas, A_i , perpendicular to the centerlines were calculated for centerline node i , with a spacing of approximately 0.5 mm.

Masking of junctions. After centerline generation, the portions of the centerlines which coincide with arterial junctions were masked in order to exclude them from the 1D domain definition, since no reasonable 1D description of such portions of the domain can be formulated. This process was performed as summarized in Algorithm 2 and explained below. Points in mother (m) and daughter vessels (d) were masked based on different criteria. Points $p_{d,1}$ and $p_{d,2}$ in daughter vessel 1 and daughter vessel 2 were considered as part of the junction if

$$S_{d_1-d_2} \leq r_{\max\text{-sphere},d_1} + r_{\max\text{-sphere},d_2}, \quad (19)$$

where $S_{d_1-d_2}$ is the distance between points $p_{d,1}$ and $p_{d,2}$ and $r_{\max\text{-sphere},d_1}$ and $r_{\max\text{-sphere},d_2}$ are the maximum inscribed sphere radius at points $p_{d,1}$ and $p_{d,2}$ respectively. A point p_m of the mother vessel was considered as part of the junction if

$$S_{m-d} \leq 1.5 r_{\max\text{-sphere},d_{\min}}, \quad (20)$$

where S_{m-d} is the distance between point p_m and a point, p_d in a daughter vessel. The value $r_{\max\text{-sphere},d_{\min}}$ for a point p_d situated n points downstream of the center of the junction is found by evaluating $r_{\max\text{-sphere}}$ for all daughter vessels at the same number of points (n) downstream the center of the junction, and taking the minimum observed value, see Fig. 3. The criteria in Eqs. (19) and (20) were designed to keep as much of the 1D-0D domain intact; however, this caused incomplete masking in some cases (particularly of centerline points in daughter vessels) as visualized in Fig. 4. In order to check for the smoothness of transition from junctions to 1D segments we calculated the ratio of the maximum inscribed sphere and radius of the cross-sectional area, $r_i = \sqrt{\frac{A_i}{\pi}}$ for successive points, i.e.

$$\gamma = \frac{\frac{r_i}{r_{\max,i}}}{\frac{r_{i+1}}{r_{\max,i+1}}}. \quad (21)$$

After the initial junction mask in step 1, γ was calculated for the next 10 downstream centerline points in daughter vessels. If γ exceeded a value of 1.3 for a centerline point, $i = n$, the centerline points $1, \dots, n$, $n < 10$ were also marked as part of the junction. Fig. 4 show the result before (left) and after (right) the correction.

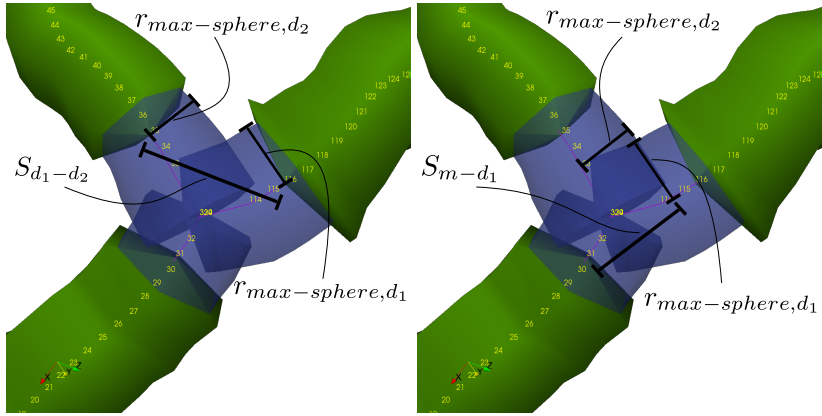


Fig. 3: Illustration of step one for detection of junctions. The green tubes correspond to radius obtained from cross-sectional area perpendicular to centerline, and blue tubes to the radius of the maximum inscribed sphere.

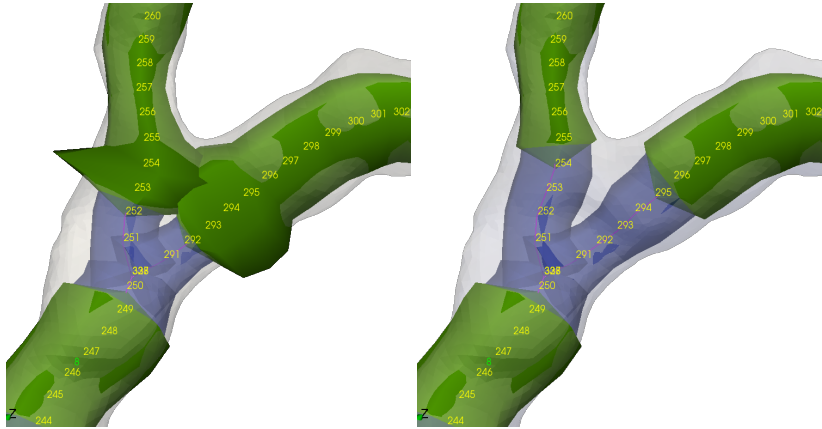


Fig. 4: Illustration of the second step for masking of junctions. The left panel illustrate the result of applying junction criteria based on Eqs. (19) and (20), whereas the right panel shows the final result after correcting with criteria based on Eq. (21)

Masking of stenotic regions. Stenotic regions are parts of the original domain where the 1D blood flow model is not valid and must be replaced by ad-hoc models for the prediction of pressure drop across stenoses. Such regions were detected and quantified by comparing the observed radius r_i to an estimated healthy radius \hat{r}_i predicted by a weighted Gaussian kernel filtering procedure on the reconstructed radius r_i . It is worth noting that the healthy radius \hat{r}_i is needed by the stenosis detection algorithm since a priori there is no reference

Algorithm 2 Junction masking algorithm

```

1: for segmentk in 1D-0Dnetwork do
2:   for pi in segmentk do
3:     for segmentl in 1D-0Dnetwork do
4:       for pj in segmentl do
5:         if segmentk is not segmentl then
6:           Calculate distance, Spi-pj, between points pi and pj
7:           if Spi-pj < rmax-sphere,pi + rmax-sphere,pj then
8:             if segmentk is not mother of segmentl then
9:               mask point pj as junction
10:            else if segmentl is daughter of segmentk then
11:              rmax-sphere,dmin ← ∞
12:              for segmentd in daughters of segmentk do
13:                if rmax-sphere,d,pj < rmax-sphere,dmin then
14:                  rmax-sphere,dmin ← rmax-sphere,d,pj
15:            Calculate distance, Spi-pj, between points pi and pj
16:            if Spi-pj < 1.5 · rmax-sphere,dmin then
17:              mask point pi as junction
18: Remove masked points from the segments in 1D-0Dnetwork
19: for segmentk in 1D-0Dnetwork do
20:   for i in range (10) do
21:     calculate γ(pi, pi+1)
22:     if γ > 1.3 then
23:       mask points p1, ..., pi as junction

```

radius available. The methodology followed here was proposed by Shazad et al. [43].

First a local average radius r_i^{\max} is calculated by averaging the observed radii according to a Gaussian kernel with standard deviation σ_{\max} , that is

$$r_i^{\max} = \frac{\sum_{i'=1}^n N(i'|i, \sigma_{\max}) r_{i'}}{\sum_{i'=1}^n N(i'|i, \sigma_{\max})}. \quad (22)$$

Here and in, what follows $i'|i$ denotes the distance between centerline nodes with indexes i and i' . Based on this smoothed radius and its deviation from the local average, a weight factor is calculated for each observed radius as

$$w_i = N(r_i | r_i^{\max}, \sigma_r). \quad (23)$$

Finally, the healthy radius is estimated by averaging the observed radii weighted by proximity, using a Gaussian kernel with standard deviation σ_x , and the likelihood, w_i , of each observed radius, r_i , given the local average r^{\max} , i.e.

$$\hat{r}_i = \frac{\sum_{i'=1}^n N(i'|i, \sigma_x) w_{i'} r_{i'}}{\sum_{i'=1}^n N(i'|i, \sigma_x) w_{i'}}, \quad (24)$$

where $N(i'|i, \sigma) = \frac{1}{\sigma\sqrt{2\pi}} \exp \{ -(i' - i)^2 / 2\sigma^2 \}$.

A centerline node was marked as a stenosis if the stenosis degree was above a stenosis threshold θ_s , where stenosis degree is defined as

$$\text{SD}_i = 1 - \frac{r_i}{\hat{r}_i}. \quad (25)$$

Stenotic regions were determined by traversing upstream and downstream of such centerline nodes and marking all nodes where SD_i was above a certain healthy stenosis threshold, θ_h . The radius associated with centerline points at the start (upstream, u) and end (downstream, d) were used to calculate the reference radius of the stenotic region according to $r_0 = 0.5(r_u + r_d)$. The stenosis model (see. Eq. 16) was then quantified by the minimum radius r_s , reference radius r_0 and stenosis length, $L_s = (x_d - x_u)$, see Algorithm 3.

Algorithm 3 Stenosis detection algorithm

```

1: Estimate healthy radius  $\hat{r}$  of 1D segment
2: Calculate SD for all points in segment
3:  $r_s \leftarrow \infty$ 
4:  $\{x_i\} \leftarrow \{x_i | \text{SD}_i > \theta_s\}$ 
5: for  $x_k$  in  $\{x_i\}$  do
6:    $x_u \leftarrow \arg \min(x_k - x_j)$  such that  $\text{SD}_j < \theta_h$ 
7:    $x_d \leftarrow \arg \min(x_j - x_k)$  such that  $\text{SD}_j < \theta_h$ 
8:   Replace the region between  $x_u$  and  $x_d$  with a stenotic junction model (see Eq. (16))
9:   if  $r_k < r_s$  then
10:     $r_s \leftarrow r_k$ 
11:     $l_s \leftarrow x_d - x_u$ 
12:     $r_0 \leftarrow 0.5(r_u + r_d)$ 

```

The determination of stenotic regions is illustrated by Fig. 5. The left panel shows the original radius r together with the estimated healthy radius, \hat{r} , for a 1D segment. Additionally, the calculated stenosis degree and a stenotic region based on a stenosis threshold, $\theta_s = 0.3$, and healthy threshold, $\theta_h = 0.2$, are shown. The right panel of the figure shows a 1D network extracted from a 3D volume mesh. The 1D segments are separated at arterial junctions, and further divided into stenotic (colored) and healthy regions (dark blue) as described above. The segment with the most severe stenosis (red) corresponds to the vessel shown in the left panel of the figure.

2.4 Uncertainty quantification and sensitivity analysis

In addition to verifying that a computational model solves the idealized mathematical model to an adequate level of accuracy and subsequently validating that it accurately represents the real system we are interested in, we must also consider how the model will perform when the inputs required to specify the system are uncertain. This is often the case, especially in biomedical modelling as many parameters and inputs appearing in our models are taken from

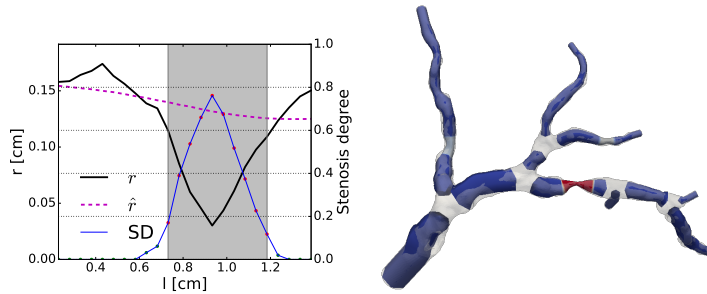


Fig. 5: Original radius, r , and estimated healthy radius, \hat{r} , together with calculated stenosis degree, SD, and the stenotic region (shaded area) for a 1D segment is shown in the left panel. A 1D network of arteries (blue) extracted from a 3D volume mesh (transparent grey), where junctions and stenotic regions have been masked is illustrated in the right panel.

population data or from patient specific measurements that may have significant variability. Uncertainty quantification and sensitivity analysis (UQ&SA) provide a means to analyze the performance of models relying on uncertain inputs, as well as assisting in prioritizing which inputs are limiting factors that prevent greater certainty in model predictions.

2.4.1 UQ&SA framework

UQ&SA were conducted to identify which parameters for model reduction were most influential and to analyze the performance of the model with clinically relevant levels of uncertainty in input data. The uncertainty in the first case represents the range of model behavior when allowing parameters to vary over some predetermined range, whereas in the second case the intention is to quantify the expected range of model predictions given the assumed uncertainties in model inputs. In both cases the first requirement is to perform UQ of the model M , which takes input data \mathbf{z} to yield a prediction y . Since the values of \mathbf{z} are unknown the uncertainty about them may be represented by a random vector \mathbf{Z} with distribution chosen to reflect the situation of interest. Thus the model output is also a random variable, $Y = M(\mathbf{Z})$.

The problem at hand is to characterize the distribution of Y given the distribution of \mathbf{Z} . We employ the nonintrusive Monte Carlo methods and Polynomial chaos to do so as these treat M as a black box and do not require modifying M to account for the stochastic nature of \mathbf{Z} . The review of Eck et al. [9] presents several methods and concepts of UQ&SA within the context of cardiovascular modelling, and we refer the reader to this work for more details regarding the methods of UQ&SA used here.

Visualization of the distribution of Y as well summary quantities such as the mean $\mathbb{E}[Y]$, variance $\mathbb{V}[Y]$ and percentiles provide a means for assessing the performance of a model under realistic conditions with uncertain inputs

and allow determining if the model uncertainty is low enough for use. For example the 2.5-th and 97.5-th percentiles ($y_{2.5\%}$, $y_{97.5\%}$), determine a range where 95 % of realizations of Y will fall given the uncertainty about \mathbf{Z} . Note that this analysis does not account for any uncertainty due to the discrepancy between the model and reality, often referred to as modelling error.

Sensitivity analysis (SA) further analyzes the distribution of Y in order to identify the contributions of particular inputs to the overall uncertainty. Understanding how distinct inputs contribute to uncertainty allows prioritization of inputs for parameter estimation or for higher fidelity measurement. Sobol sensitivity indices, first-order (S_i) and total ($S_{T,i}$), are widely employed [40], defined as

$$S_i = \frac{\mathbb{V}[\mathbb{E}[Y | Z_i]]}{\mathbb{V}[Y]} \quad (26a)$$

$$S_{T,i} = 1 - \frac{\mathbb{V}[\mathbb{E}[Y | \mathbf{Z}_{-i}]]}{\mathbb{V}[Y]}, \quad (26b)$$

where the vector, \mathbf{Z}_{-i} , contains all elements of \mathbf{Z} except Z_i . These indices partition the total $\mathbb{V}[Y]$ into portions attributable to specific combinations of inputs. The first order indices S_i quantify the variance due to Z_i alone, i.e. independent of the values of the other inputs. The total sensitivity index, $S_{T,i}$, includes effect due to interaction with other parameters and represents the reduction in variance expected to be achieved by fixing Z_i at a particular value.

Larger values of S_i suggest that Z_i strongly affects Y and thus may be a prime target for improved measurement or optimization in the context of parameter estimation. In the case where $S_{T,i}$ and thus also S_i are small, Z_i has little influence on Y and should not be prioritized for improved measurement and may not be estimated accurately in an inverse problem context. When S_i is small but $S_{T,i}$ is large, the effect of Z_i depends greatly on the values of other parameters thus it may still be valuable to improve its measurement, and it may be estimated in an inverse problem though its identifiability may depend on the values of other parameters.

In many cases M does not simply model a single scalar value, but a vector, or even a continuous function. While the above methods and indices still apply pointwise, it is often useful to summarize the uncertainties and sensitivities. Eck et al. [10] proposed a method to summarize sensitivities of time varying quantities by weighting the sensitivities by the uncertainty, $\mathbb{V}[Y]$, at each time point. This may naturally be extended to any set or region where the sensitivities are desired to be summarized by a weighted average over the points of interest.

These averaged sensitivities are based on comparing the sensitivities between two points based on weighting by the uncertainty at those points

$$V_i^k = \mathbb{V}[\mathbb{E}[Y_k | Z_i]] = S_i^k \mathbb{V}[Y_k]. \quad (27a)$$

$$V_{T,i}^k = \mathbb{V}[\mathbb{E}[Y_k | \mathbf{Z}_i]] = S_{T,i}^k \mathbb{V}[Y_k]. \quad (27b)$$

where S_i^k and $S_{T,i}^k$ are respectively the first order and total sensitivity index of output Y_k with respect to Z_i . This weighting partitions the uncertainty according the particular inputs but, in contrast to S_i and $S_{T,i}$, allows comparison based on the absolute amount of uncertainty due to input Z_i at each point rather than the normalized proportion. Thus input Z_j may have a high sensitivity at point k , but the uncertainty at k may be very small. Thus one must consider if the absolute uncertainties should be compared or only the normalized sensitivities.

From V_i^k and $V_{T,i}^k$ the averaged first-order sensitivity indices are calculated as

$$AS_i = \frac{\sum_{k=1}^n V_i^k}{\sum_{k=1}^n \mathbb{V}[Y]_k} = \frac{\sum_{k=1}^n S_i^k \mathbb{V}[Y_k]}{\sum_{k=1}^n \mathbb{V}[Y_k]}, \quad (28)$$

and averaged total sensitivity indices are

$$AS_{T,i} = \frac{\sum_{k=1}^n V_{T,i}^k}{\sum_{k=1}^n \mathbb{V}[Y]_k} = \frac{\sum_{k=1}^n S_{T,i}^k \mathbb{V}[Y_k]}{\sum_{k=1}^n \mathbb{V}[Y_k]}. \quad (29)$$

These may provide useful summaries of sensitivities, particularly when the uncertainties of the various outputs of M are quite different.

To perform UQ&SA for a given model one must first specify the uncertainty of the inputs by specifying an appropriate distribution for \mathbf{Z} . The distribution should reflect the conditions the UQ&SA is intended to analyze, thus for evaluating model performance, one should choose inputs reflecting the actual uncertainties of the inputs that will be used when employing the model. On the other hand, when performing UQ&SA to analyze a model's range of behavior and to identify inputs relevant for input estimation, the distribution of \mathbf{Z} should reflect the range of plausible values for the inputs. For instance, if only a range of values is considered and no prior knowledge is available to prioritize certain regions, a uniform distribution is appropriate to investigate how the inputs influence the model's behavior.

Once the distribution \mathbf{Z} has been specified, the method to approximate the measures of uncertainty and sensitivity indices must be determined, a decision affected by the number of inputs and the smoothness of M . Noninvasive methods are typically sample based methods, e.g. Monte Carlo and Polynomial chaos with stochastic collocation or numerical quadrature. For details about these methods see [9] and references cited therein. Polynomial chaos is highly efficient relative to Monte Carlo as long as M is sufficiently smooth and is thus preferred when applicable. Both approaches approximate $Y = M(\mathbf{Z})$ by evaluating the deterministic model $y = M(\mathbf{z})$ at each sample point in $\{\mathbf{z}^{(s)}\}_{s=1}^{N_s}$, which is a set of points sampled from the input distribution \mathbf{Z} or determined by the specific approximation algorithm used. Once the values of M are calculated for each sample point the estimated measures of uncertainty and sensitivity are computed according to the specific method chosen. The accuracy of the methods is typically not assessed a priori and thus a posterior estimate of the error is necessary to assess convergence. For Monte Carlo methods bootstrapping is often used to assess the precision of the

estimates [36]. The samples $\{y^{(s)}\}_{s=1}^{N_s}$ are resampled to generate a number of new sample sets. For each of these sample sets the measures of uncertainty and sensitivity are calculated and the statistics of the set of estimated measures provide an assessment of the accuracy achieved.

2.4.2 UQ&SA for 1D-0D model setting

The hybrid 1D-0D model described in Sect. 2.3 is based on a series of assumptions. The governing equations for blood flow given by Eqs. (13a)-(13b) assume an axisymmetric vessel and negligible radial velocity component. The axial velocity component still has a radial dependence, however, the shape of the velocity profile must be specified a priori in the derivation of Eq. (13b). In this work we have assumed a power law profile given by Eq. (14), where ζ is the polynomial order, and defines the shape of the profile. Though this velocity profile is commonly used, little work has focused on what value of ζ is appropriate for blood flow in human arteries. In [45] a value $\zeta = 9$ was used in an anatomically based model of coronary blood flow, whereas values of $\zeta = 2$ (carotid artery), and $\zeta = 9$ (aorta) were used in a systematic comparison between 1D and 3D hemodynamics in [52].

At arterial junctions and more importantly at stenotic regions, the assumptions of unidirectional blood velocity is no longer valid. In order to identify such regions, the coronary geometry is preprocessed as described in Sect. 2.3.1. The healthy vessel radius estimation uses a Gaussian kernel filtering procedure, Eq. (24), that depends on parameters σ_x (corresponding to centerline longitudinal distance), σ_r (corresponding to radius) and σ_{\max} . In [43], where centerline dimensions are given in millimeters, σ_x , σ_r and σ_{\max} were set to 8 mm, 0.25 mm and 200 mm respectively. In this work we have related the parameters to the maximum radius r_{\max} of the vessel of interest such that $\sigma_x = r_{\max} \sigma_x^*$, $\sigma_r = r_{\max} \sigma_r^*$ and $\sigma_{\max} = r_{\max} \sigma_{\max}^*$. Given the estimate of healthy vessel radius, the determination of stenotic regions depends on θ_s and θ_h . The stenosis threshold, θ_s , defines how severe a stenosis has to be before a region is marked as stenotic. A value of $\theta_s = 0$ would classify all regions with a positive stenosis degree as stenosis, whereas no regions would be classified as stenotic for a value of $\theta_s = 1$. The stenosis healthy threshold, θ_h , defines the length of the stenotic region. In this work, we have linked θ_h to θ_s such that $\theta_h = \theta_h^* \theta_s$, where $0 \leq \theta_h^* \leq 1$. See Fig. 5 for an illustration of the stenosis detection procedure.

The stenosis detection procedure labels regions as healthy or stenotic. The 1D equations for blood flow given by Eqs. (17a)-(17b) are applied in healthy regions, while stenotic regions are modeled using Eqs. (15a)-(16). The second term of Eq. (16), which reflects the pressure drop due to a sudden expansion, includes the parameter K_t . A value of $K_t = 1$ reflects a uniform outlet velocity, whereas a value of $K_t = 1.52$ reflects the product of a uniform and constant outlet velocity [18].

In order to identify the most relevant parameters in the construction of the reduced order model described in Sect. 2.3 we performed a sensitivity analysis

Table 1: Ranges for exploratory sensitivity analysis of the hybrid 1D-0D model (Sect. 2.3). Uniform distributions with minimum and maximum values denoted below were assigned to all parameters. All parameters are dimensionless.

Input	Symbol	Minimum	Maximum
Flow profile order	ζ	2	9
Local averaging kernel length	σ_x^*	0.1	3
Healthy radius variability	σ_r^*	0.0075	1.5
Healthy smoothing kernel length	σ_{\max}^*	3	8
Diseased threshold	θ_s	0	1
Healthy threshold	θ_h^*	0	1
Turbulent Loss coefficient	K_t	1	2

for the uncertain parameters $\mathbf{Z}_{3D \rightarrow 1D} = [\zeta, \sigma_x^*, \sigma_r^*, \sigma_{\max}^*, \theta_s, \theta_h^*, K_t]$. Parameters variation was described by using uniform distributions with limits based on the plausible ranges of each parameter (see Table 1 for exact ranges). Sensitivity analysis was performed individually for all ($N = 248$) 1D segments (including three or more centerline points), and with $y = M(\mathbf{z}) = \Delta P_{1D-0D}(z)$. The flow rate, Q , for each segment was taken from the solution obtained using the 3D modeling framework. Then, ΔP_{1D-0D} was obtained by evaluating Eqs. (17b) and (16) as defined by \mathbf{z} and with Q as input.

Measures of uncertainty and sensitivity were estimated by the Monte Carlo method as described by Saltelli [39], and the accuracy of UQ&SA results was assessed by evaluating the standard deviation of the estimates from 10 bootstrapped samples until the standard deviation was below 0.0033 (i.e. 99 % confident that obtained value is within ± 0.01 , with assumptions of normality) for all sensitivity indices with an estimated value larger than 0.05. The maximum number of model evaluations was 3,121,812.

2.4.3 UQ&SA for FFR prediction setting

Conducting blood flow simulations for estimation of FFR as described in Sect. 2.2 requires determination of parameters based on clinical imaging, patient-specific characteristics, clinical measurements and values from literature (population based studies, physiological studies, etc.). We apply uncertainty quantification and sensitivity analysis to understand the effect of uncertain input parameters on FFR predictions for all available (24) invasive FFR measurements.

An estimate of mean aortic pressure is [37]

$$\text{MAP} = \frac{2}{3}P_d + \frac{1}{3}P_s. \quad (30)$$

A standard deviation in diastolic pressure, P_d , of 5.5 mmHg and a standard deviation in systolic pressure, P_s , of 3.3 mmHg were reported in [16]. By assuming perfect positive correlation between P_d and P_s , a standard deviation in the estimated aortic pressure is 4.77 mmHg. By these considerations, we

modeled the estimate of aortic pressure (used as inlet boundary condition in the FFR predictions) as a normal variable with mean given by Eq. (30) and with a standard deviation of 4.77 mmHg.

Cardiac output (CO) was estimated (CO_{meas}) based on cross-sectional area and velocity-time integral at the left ventricle outflow tract derived from PW Doppler [25]. Dubin et al. [8] compared echocardiographic estimates of cardiac output to thermodilution-derived invasive estimates. The average difference between the two methods was 0.11 L/min with a standard deviation of 0.69 L/min. Thus, the uncertainty in CO based on the measurement, CO_{meas} , is modeled by a normally distributed random variable with mean corresponding to the PW Doppler estimate of CO_{meas} and a standard deviation of 0.69 L/min.

The flow split between left and right coronary branches is based on the work of Sakamoto et al. [38], who studied coronary blood flow to the Left Anterior Descending (LAD), Left Circumflex (LCX) and the Right Coronary Artery (RCA) in relation to coronary artery dominance. The resulting average flows and standard deviations quantify the expected range of flow fractions to the left and right coronary trees based on the dominance of the individual. Sakamoto et al. [38] report mean and standard deviation of absolute flow to each coronary branch but do not account for differences in variability due to differences in cardiac output or total coronary flow. We thus assume that the flow to each branch is an independent fraction of CO and that the variability for individuals with a given CO is proportional to the CO. Thus, the reported absolute flows and standard deviations are normalized by the population average cardiac output, 6 L/min, in order to produce the corresponding flow fractions as given in Table 2. Note that this allows us to combine the uncertainty related to the percent of CO to the coronaries and the separate factor for the flow to each branch, γ_k^j , while still having an expected total coronary flow of approximately 4.5 %.

Blood density and viscosity are related to the hematocrit level. We adopt the relation for viscosity reported in Sankaran et al. [41], where $\mu = \frac{\mu_p}{(1-H)^{2.5}}$, with $\mu_p = 0.001 \text{ Pa}\cdot\text{s}$ the viscosity of plasma and H the hematocrit level. With this we modeled H as normal variable with a mean of 0.45 and a standard deviation of 0.031 based on average population variations [51]. The density of blood can be related to the hematocrit according to $\rho = \rho_e H + (1 - H) \rho_p$, where $\rho_p = 1018 \text{ kg/m}^3$ is the density of plasma, and $\rho_e = 1085 \text{ kg/m}^3$ is the density of erythrocytes [23].

The total peripheral resistance was distributed among outlets using Murray's law [32], which has a theoretical exponent of $c = 3$, derived from the principle of minimum work. More recent studies [17] have suggested an exponent of $c = 7/3$. We modeled Murray's exponent as a uniform variable where $2.0 \leq c \leq 3.0$.

The coronary arteries were segmented semi-automatically from the CT images using ITK-SNAP. The software requires one to set upper and lower thresholds for intensities (Houndsfield units) that define what is considered coronary vessel lumen. A larger lower threshold will decrease the cross-section

Table 2: Input uncertainties for evaluation of the effects of parametric input uncertainty on 1D-0D estimates of FFR. Uniform distributions are denoted by $\mathcal{U}(\min, \max)$ and normal distributions $\mathcal{N}(\text{mean}, \text{std. dev.})$. The gamma distribution for α is denoted by $\mathcal{G}(\text{shape}, \text{scale})$. The measured cardiac output is denoted CO_{meas} . Mean aortic pressure is represented as P_{meas} , and it is obtained from measurements and Eq. (30). We include coronary flow fraction distributions for each the four possible combinations of branch and dominance, but note only one was used for any given case.

Input	branch, dominance	Symbol	Distribution
Cardiac Output	-	CO (L/min)	$\mathcal{N}(CO_{\text{meas}}, 0.69)$
Arterial Pressure	-	MAP (mmHg)	$\mathcal{N}(P_{\text{meas}}, 4.77)$
Coronary flow fraction	left, right	λ_{cor} (%)	$\mathcal{U}(1.78, 3.42)$
Coronary flow fraction	right, right	λ_{cor} (%)	$\mathcal{U}(1.1, 2.7)$
Coronary flow fraction	left, left	λ_{cor} (%)	$\mathcal{U}(2.7, 4.1)$
Coronary flow fraction	right, left	λ_{cor} (%)	$\mathcal{U}(0.27, 1.6)$
TCRI	-	α (-)	$\mathcal{G}(3, 0.75)$
Murray's law exponent	-	c (-)	$\mathcal{U}(2.0, 3.0)$
Hematocrit	-	H (-)	$\mathcal{N}(0.45, 0.031)$
Stenosis radius perturbation	-	Δr_s (mm)	$\mathcal{U}(-0.1, 0.1)$
Stenosis length factor	-	λ_{L_s} (-)	$\mathcal{U}(-0.2, 0.2)$

of the segmented lumen, whereas a smaller lower threshold would have the contrary effect. Such variations in lumen cross-section is particularly important at stenotic regions. To account for this, we introduced a global parameter Δr_s to be applied to all stenotic regions of a network such that the minimum radius in stenotic regions was given by $r_s = r_{s,\text{segmented}} + \Delta r_s$, where $r_{s,\text{segmented}}$ is the minimum radius as obtained from the original segmentation. The minimum $r_{s,\text{segmented}}$ in our population was 0.29 mm, and we modeled Δr_s as a uniform variable ranging from -0.1 mm to 0.1 mm. Similarly, we modeled the stenotic length as $L_s = (1 + \lambda_{L_s}) L_{s,\text{segmented}}$, where λ_{L_s} is assumed to follow a uniform distribution between -0.2 to 0.2.

Coronary flow can increase significantly with respect to resting flow during hyperemic conditions. Vasodilation of peripheral vessels downstream from epicardial arteries is the most important mechanism controlling coronary flow [46]. Such changes can be seen as variations in the so-called total coronary resistance index α . Although α is difficult to measure, it is related to the Coronary Flow Reserve (CFR), which is the ratio of flow in hyperemic and baseline conditions. According to the meta-analysis by Johnson et. al. [21], CFR is normally between 1 and 6 with an average value of 2.57 for non-ischemic vessels. The distribution is akin that of the gamma [29]. From these considerations, we modeled the hyperemic factor α as a gamma distribution with shape parameter 3, scale-factor 0.75 and shifted to 1.

We performed uncertainty quantification and sensitivity analysis for FFR predictions from the reduced order model described in Sect. 2.3 for 24 locations where FFR was measured invasively. Parameters that are related to the process of going from a 3D problem to a 1D-0D model are those deriv-

ing from the sensitivity analysis described in Sect. 2.4.2 and an optimization procedure based on such analysis. The pipeline for predicting FFR was the same as outlined in Sect. 2.2.2, however, now with the input parameters $\mathbf{Z}_{\text{FFR}} = [\text{CO}, \text{MAP}, \lambda_{\text{cor}}, c, \alpha, H, \Delta r_s, \lambda_{L_s}]$ defined by the input distribution \mathbf{Z}_{FFR} as described above and summarized in.

The Python package `chaospy` [12] was used to calculate polynomial chaos approximations of model predicted FFR. Regression was used to estimate the coefficients of the approximations for model evaluations at points sampled according to the Hammersley sequence, which allows for adaptively increasing the number of samples evaluated. The number of points used for each order of approximation was twice the number of terms in the expansion. The accuracy of the results from UQ&SA was assessed by comparing the estimates between successive orders of approximation until the difference between estimated sensitivity indices was below 0.01 for all indices with an estimated value larger than 0.05. A approximation of maximum order 7 was performed, which required 12,870 samples.

Cases that required approximation order greater than 7 were computed more efficiently in terms of computational burden by the Monte Carlo method as described by Saltelli [39], and the accuracy of UQ&SA results was assessed by evaluating the standard deviation of the indices from 10 bootstrapped samples until the standard deviation was below 0.0066 (i.e. 99 % confident that obtained value is within ± 0.02 , with assumptions of normality) for all sensitivity indices with an estimated value larger than 0.05. The maximum number of model evaluations was 1,775,970.

3 Results

3.1 3D simulation results

While the primary objective of this work is to present and analyze a 1D-0D framework for model-based FFR prediction, we report here the comparison of predicted FFR values obtained using the 3D modeling framework described in 2.2.2 versus invasive measured FFR values. Such values are provided in order to show that the FFR prediction modeling framework, while still under development, provides results that are aligned with many publications on model-based FFR prediction, specially for initial stages of model development. The average error of FFR predictions was -0.033 and the standard deviation of the error was 0.119. Moreover, the correlation coefficient of predicted FFR versus invasive FFR was 0.84. In terms of diagnostic accuracy, prediction sensitivity, specificity, positive predicted value and negative predicted value were 60 %, 93 %, 86 % and 76 %, respectively. Fig. 6 shows a scatter plot and a Bland-Altman plot for predicted FFR versus measured FFR. More relevant for the current study are results reported in Fig. 7, that shows predicted FFR based on steady state simulations versus predicted FFR based on transient

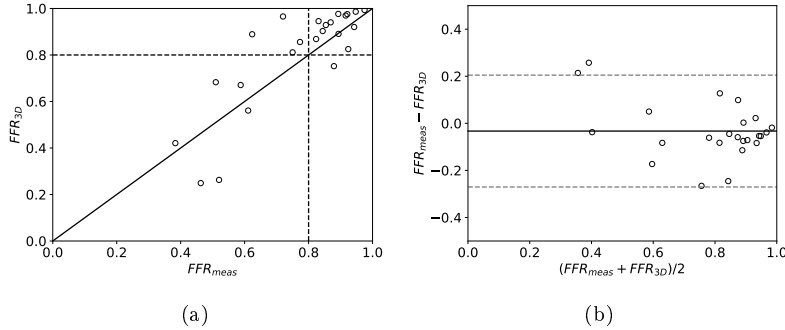


Fig. 6: Predicted FFR, FFR_{3D} , versus invasive FFR, FFR_{meas} . Scatter plot with grey line showing the FFR cutoff value of 0.8 (left) and Bland-Altman plot with dashed lines showing ± 2 standard deviations (right).

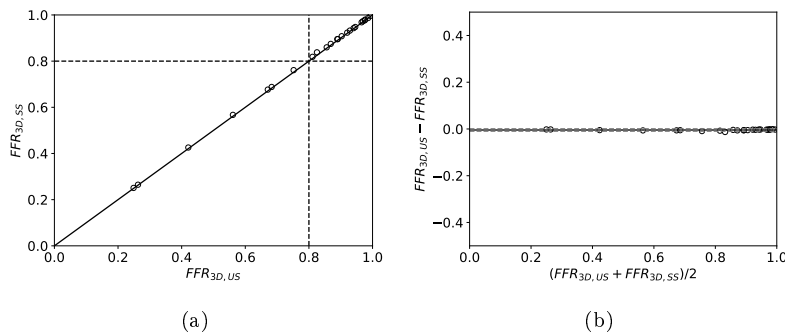


Fig. 7: Predicted FFR based on steady state simulations, $FFR_{3D,ss}$, versus predicted FFR based on transient simulations, $FFR_{3D,us}$. Scatter plot with grey line showing the FFR cutoff value of 0.8 (left) and Bland-Altman plot with dashed lines showing ± 2 standard deviations (right).

simulations. In this case, mean error was -0.004 and standard deviation of the error was 0.003, with a correlation coefficient of 1.00.

3.2 Design and validation of the reduced order model for coronary blood flow simulations

3.2.1 Sensitivity analysis

We performed sensitivity analysis as described in Sect. 2.4.2 in order to identify most influential parameters in the construction of the reduced order model described in Sect. 2.3. The sensitivity analysis was performed for each of the

248 coronary vessel segments to estimate first-order (S_i) and total ($S_{T,i}$) Sobol sensitivity indices for each case. The average sensitivities for all cases are presented in Table 3 and show that the velocity-profile parameter ζ is by far the most influential parameter for most of the cases, with an average $S_{T,\zeta}$ of 0.88. The second most influential parameter is θ_s , which determines the marking of stenotic regions and has an average S_{T,θ_s} of 0.13. Moreover, aggregated sensitivities, AS_i and $AS_{T,i}$, where the individual uncertainties, $\mathbb{V}[Y]$, are taken into account are also shown in Table 3 and show that weighting the sensitivities with the uncertainty leads to a different ranking in terms of most influential parameters. The stenosis threshold is the parameter that contributes the most aggregate sensitivity, with $AS_{T,\theta_s} = 0.65$. Second most influential is σ_x^* , followed by ζ and θ_h^* .

Table 3: Summary of sensitivities resulting from the analysis in Sect. 2.4.2. The average first-order (S_i) and total ($S_{T,i}$) sensitivity indices (see Eqs. (26a) and (26b)), and the uncertainty weighted first-order (AS_i) and total ($AS_{T,i}$) sensitivity indices are reported (see Eqs. (28) and (29)).

	ζ	σ_x^*	σ_r^*	σ_{\max}^*	θ_s	θ_h^*	K_t
S_i	0.867	0.006	0.001	0.000	0.074	0.001	0.001
$S_{T,i}$	0.881	0.040	0.021	0.004	0.126	0.019	0.005
AS_i	0.164	0.118	0.007	0.000	0.471	0.026	0.017
$AS_{T,i}$	0.171	0.277	0.064	0.009	0.653	0.088	0.032

The results from the sample based sensitivity analysis described in Sect. 2.4.2 were also analyzed in terms of the residuals $res = \Delta P_{3D} - \Delta P_{1D-0D}(z)$. In particular, cases where no realization of $\Delta P_{1D-0D}(z)$ in the broad range defined by $Z_{3D \rightarrow 1D}$ yielded residuals lower than 7.5 mmHg were inspected in detail. Such segments were either associated with a moderate to severe stenosis with non-cylindrical shape and abrupt changes in radius, i.e. calcified stenosis, or multiple mild stenoses with non-cylindrical shape.

3.2.2 Identification of optimal parameters

We performed optimization to estimate the values of the four most influential parameters ($\theta_s, \sigma_x^*, \zeta$ and θ_h^*) based on $AS_{T,i}$. The remaining parameters were fixed: $\sigma_r^* = 1$, $\sigma_{\max}^* = 4$ and $K_t = 1.52$. We used the Python package `scipy` to perform parameter estimation. A grid search approach, `scipy.optimize.brute`, was chosen due to the discontinuous character of the problem in terms of stenosis identification and inability of other algorithms to provide meaningful results. In order to enhance identifiability we separated the optimization into two cohorts, one in which the parameters related to the stenosis detection were estimated, and one in which ζ was optimized. In the first cohort (N=19 vessel segments), all vessel segments with $V_{T,\theta_s}^k > 1$ mmHg (See Eq. (27b)) were included, i.e. vessel segments where the square root of the variance due

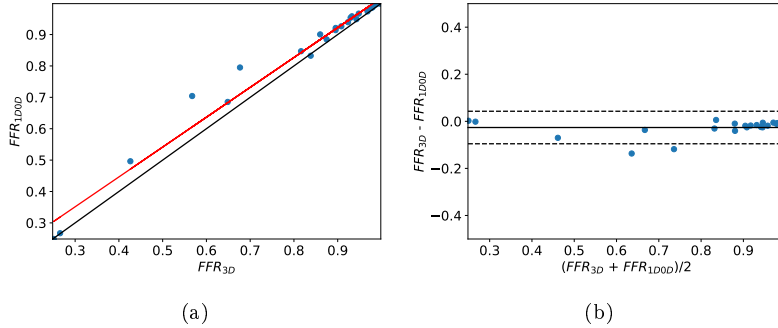


Fig. 8: Comparison of FFR_{1D-0D} and FFR_{3D}. Scatter plot (left) and Bland-Altman plot (right). The reduced order model had a bias of $\text{FFR}_{3D} - \text{FFR}_{1D-0D} = -0.03$ and a standard deviation of 0.03

to θ_s contributed to 1 mmHg or more. In the second cohort ($N=213$ vessel segments), all vessel segments with $V_{T,\theta_s}^k < 0.1$ mmHg were included and used to estimate ζ . The root mean square error was used as cost function in the parameter optimization, defined as

$$\epsilon = \sqrt{\frac{1}{N} \sum_{k=1}^N (\Delta P_{3D}^k - \Delta P_{1D-0D}^k)^2} \quad (31)$$

with N the number of vessel segments in the optimization procedure, ΔP_{3D}^k the pressure drop in vessel segment k obtained with the 3D model framework, and ΔP_{1D-0D}^k the pressure drop obtained using the 1D-0D model. Optimized parameters are shown in Table 4, and Fig. 8 shows predicted FFR from 1D-0D model (applying optimized parameters) vs predicted FFR from 3D model framework at locations where FFR was measured. Equivalent inlet (pressure) and outflow (resistance) boundary conditions were employed as defined in Sect. 2.2.2. The mean difference between FFR_{3D} and FFR_{1D-0D} was -0.03 and standard deviation was 0.03. Indeed, the two worst residuals were associated with vessel segments with non-cylindrical shape and abrupt changes in radius, as identified through analysis of residuals (see previous section).

Table 4: Optimal parameters for 1D-0D model settings. Estimated values are indicated in bold. All parameters are non-dimensional.

Parameter	ζ	σ_x^*	σ_r^*	σ_{\max}^*	θ_s	θ_h^*	K_t
Optimal/default value	4.31	2.32	1	4	0.13	0.90	1.52

Table 5: Average first-order (S_i) and total ($S_{T,i}$) Sobol sensitivity indices for the sensitivity analysis described in Sect. 2.4.3.

	CO	MAP	λ_{cor}	c	α	H	Δr_s	λ_{L_s}
S_i	0.073	0.006	0.146	0.003	0.455	0.079	0.168	0.001
$S_{T,i}$	0.093	0.007	0.179	0.003	0.510	0.091	0.187	0.002
AS_i	0.077	0.004	0.127	0.002	0.396	0.019	0.337	0.002
$AS_{T,i}$	0.086	0.004	0.139	0.002	0.420	0.021	0.361	0.002

3.3 UQ&SA for FFR prediction

3.3.1 Sensitivity analysis

We performed UQ&SA based on the uncertain input parameters

$\mathbf{Z}_{\text{FFR}} = [\text{CO}, \text{MAP}, \lambda_{\text{cor}}, c, \alpha, H, \Delta r_s, \lambda_{L_s}]$ at 24 locations where FFR was measured invasively, as described in Sect. 2.4.3. Average first-order (S_i) and total ($S_{T,i}$) Sobol sensitivity indices are summarized in Table 5 together with weighted first-order (AS_i) and total ($AS_{T,i}$) Sobol sensitivity indices. Both sets of indices indicate that uncertainties due to inlet pressure, MAP, Murray's exponent, c , and stenosis length, λ_{L_s} , have low influence on predicted FFR for the studied population, model framework, and assumed input uncertainties. Only the indices of α , H and Δr_s vary significantly between the two sets, where the sensitivity of Δr_s increases when the uncertainty in model output, $\mathbb{V}[Y]$ is taken into account. The contrary is valid for H . In other words, the uncertainty in FFR is lower in the cases where H has a high influence as compared with cases where Δr_s has a high influence. The hyperemic factor α is the most influential parameter according to both sensitivity indexes, followed by the uncertainty in minimum radius, Δr_s . Sensitivity indices are also visualized in the top row of Fig. 9, where averaged sensitivity analysis for all 24 locations are considered. The bottom row of the same figure shows average and weighted sensitivity indices for cases ($N=11$) where FFR was in the critical region $0.7 < \text{FFR}_{\text{meas}} < 0.9$. The most significant difference is seen in sensitivity to Δr_s , which is lower when only FFR values in this range are considered.

The top part of Fig. 10 shows the effect of uncertainty in input parameters on predicted FFR in terms of the mean $\mathbb{E}[Y]$ (blue circles) together with the 95 % prediction interval for all measured locations. The FFR obtained from the 3D framework and 1D-0D model with equivalent inflow and outflow boundary conditions are also shown for comparison. In the bottom part of the figure parameters CO, λ_{cor} and α are fixed at their nominal values. The horizontal lines represent \pm two standard deviations (std. dev. = 0.02) of repeated FFR measurements [20], i.e. 95 % probability of a FFR measurement error smaller than this under assumption of normality.

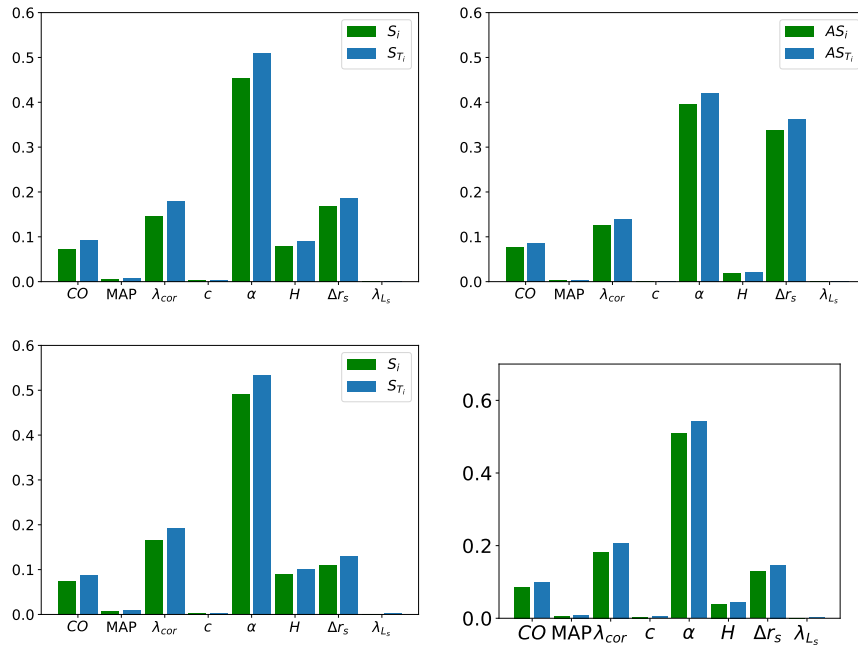


Fig. 9: The average first-order (S_i) and total ($S_{T,i}$) sensitivity indices (see Eqs. (26a) and (26b)), and the uncertainty weighted first-order (AS_i) and total ($AS_{T,i}$) sensitivity indices are reported (see Eqs. (28) and (29)). The top two bar-plots represent sensitivities when all 24 cases were considered, whereas in the bottom two, only cases ($N=11$) where FFR was in the critical region $0.7 < \text{FFR}_{\text{meas}} < 0.9$ were considered.

4 Discussion

4.1 Steady state versus transient simulations

A key aspect for the design of our 1D-0D solver in terms of computational cost is the validity of the assumption that transient terms are negligible. This also impacts model complexity, as the steady state problem allows one to avoid having to model vessel deformation in the context of 1D models. Previous works support the validity of such an assumption [30, 5]. Our results confirmed that steady state simulations can accurately reproduce FFR predictions obtained using transient models and thus allowed us to proceed with the much simpler and computationally cheaper steady state 1D-0D model with respect to the transient 1D-0D model. Of course, using a transient 1D-0D model would have resulted in enormous savings in terms of computational time with respect to transient or even steady state 3D simulations. However, the computational time would still have been prohibitive to the extensive application of UQ&SA

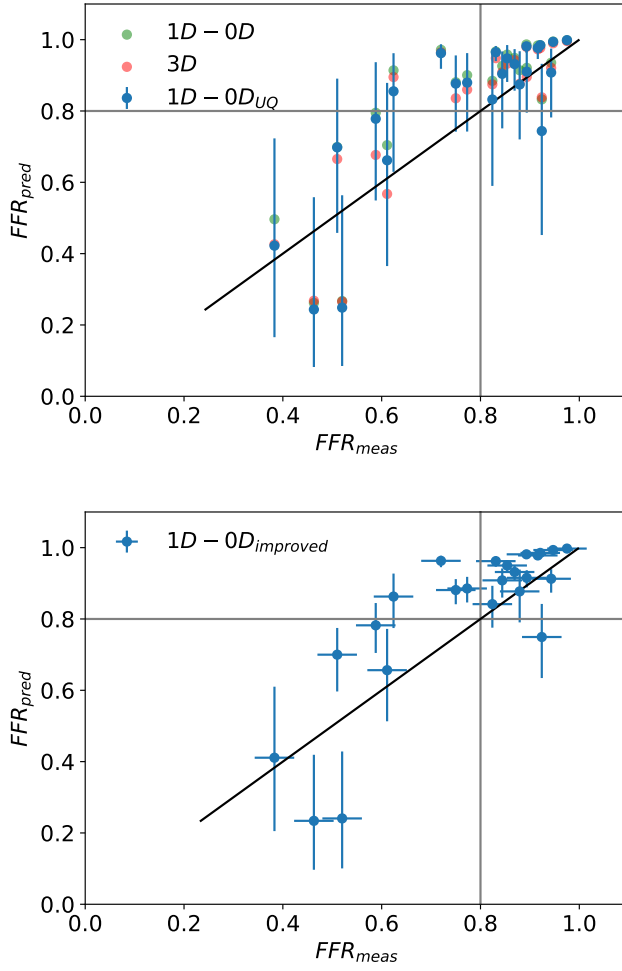


Fig. 10: The mean predicted FFR, $\mathbb{E}[Y]$, versus invasive FFR. The error bars represent the 95 % prediction intervals. The top part of the figure represent the impact of all input parameters with assumed uncertainties as described in Sect. 2.4.3, whereas all input parameters related to flow (CO, λ_{cor} and α) are fixed at their nominal values in the bottom figure. Here we also include the uncertainty in FFR (horizontal lines) represented as \pm two standard deviations (std. dev. = 0.02) of repeated FFR measurements [20]

techniques used in this work. CPU time per FFR prediction using the proposed steady state 1D-0D model was approximately 0.05 sec.

4.2 Validation of the 1D-0D modeling framework for FFR prediction

In this study we have presented a framework for conducting blood flow simulations for estimation of FFR based on clinical imaging and patient-specific characteristics. Furthermore, two different modeling approaches have been considered, the first of which is based on the transient/steady state 3D incompressible Navier-Stokes equations in rigid domains, whereas the second is based on a hybrid 1D-0D model, where healthy segments are modeled using the 1D equations for blood in axisymmetric arteries, and stenotic regions are modeled by an experimentally derived model for stenosis [26]. Fully 1D or even 1D-0D models for FFR prediction have been previously proposed in the literature [2, 3]. However, this study is distinct in that we consider a fast steady state version of the model and perform an extensive sensitivity analysis focusing on the model parameters that are related to the model reduction (i.e. going from a 3D to a simplified 1D-0D problem). We considered two parameters associated with necessary assumptions in the 1D-0D equations, namely the radial dependence of the velocity profile, represented by ζ in Eq. (17b) and the parameter K_t associated with the pressure drop due to a sudden expansion. In addition, five parameters related to the detection and quantification of stenotic regions were considered. This preprocessing of the 3D domain is necessary in order to separate the coronary tree into healthy segments where the assumptions of 1D equations for blood flow are sufficiently accurate, and stenotic regions where the assumptions do not longer hold and stenosis models have to be used.

Through the SA of given input parameters $\mathbf{Z}_{3D \rightarrow 1D}$ we found that the velocity profile parameter, ζ , was the most influential parameter. This is natural since most vessel segments were relatively smooth/healthy. However, by weighting the sensitivities by the uncertainty according to Eqs. (28) and (29) we found that the stenosis threshold, θ_s , is the most influential parameter with σ'_x , ζ and θ_h following thereafter. These parameters were then estimated by separating vessels used in the optimization procedure into two different cohorts. The filter and stenosis detection parameters θ_s , σ'_x and θ_s were estimated from cases with high variance related to stenosis threshold θ_s . The parameter ζ was estimated in a cohort of cases where θ_s had low variance (i.e. in smooth vessels). Optimal parameters were found by minimizing difference between pressure drops calculated by using the 3D modeling framework and the 1D-0D model. Little work has focused on estimating appropriate velocity profile shape, ζ , in Eq. 14 in coronary arteries by means of 3D solutions [2]. Though such a profile is commonly assumed in studies focusing on pulse wave propagation, values such as of $\zeta = 2$, Poiseille flow, or $\zeta = 9$, a plug like shape, [52, 45] are commonly used. For the cases considered, we found that the optimal value was $\zeta = 4.31$, which is between both values reported in the literature.

Furthermore, through the analysis of residuals between ΔP_{3D} and ΔP_{1D-0D} , we were able to differentiate between errors resulting from poor choices of parameters in the construction of the reduced order model, and cases where the applied models no longer hold. We acknowledge that the 1D equations are not valid at stenotic regions, and account for this by identifying and replacing such regions with a stenosis model. However, the model under consideration was developed based on experiments on idealized stenotic geometries [53], and as proven, has limited validity in severely calcified stenoses with non-cylindrical shape and abrupt changes in radius. Future work should focus on accounting for such 3D effects.

FFR predictions obtained using the reduced order 1D-0D model, employing optimized parameters, are compared with FFR predictions obtained using the 3D framework with equivalent inlet and outlet boundary conditions, see Fig. 8. General agreement was satisfactory, with a bias of $FFR_{3D} - FFR_{1D-0D} = -0.03$ and a standard deviation of 0.03. Moreover, it is worth noting that the mismatch between both modeling approaches is normally significantly smaller than uncertainties in FFR prediction due to FFR model setup (CO, α , etc), see Fig. 8. This considerations lead to evidence that even if the 1D-0D model output does not perfectly match 3D model output, it might lead to more accurate FFR predictions by allowing to explore FFR model parameters more extensively in order to design modeling setups that result in reduced uncertainty. Also predicted FFR errors with respect to measured FFR can be reduced because the lower computational cost of the 1D-0D model with respect to the 3D modeling framework might allow to obtain improved FFR modeling assumptions due to the increased capacity to explore such assumptions.

4.3 UQ&SA of predicted FFR

We attempted to characterize FFR prediction uncertainty based on uncertainty of clinical measurements (CO, MAP), and assigning conservative estimates for non-measured inputs (α , λ_{cor} , H , c). Geometric uncertainty was also included in terms of variations on minimum stenosis radius r_s and stenosis length L_s .

The hyperemic factor α has shown to be the most influential parameter, for the assumed input uncertainty and modelling framework. α represents the effect of adenosine on total coronary resistance, i.e. the factor by which peripheral resistance is reduced from baseline to hyperemic conditions. However, it is the corresponding increase of blood flow, coronary flow reserve (CFR), which is important. Fig. 11 shows the predicted mean values of CFR vs the predicted mean values of FFR. The error bars represent the ranges for the 95 % prediction interval. The average mean value of CFR was 2.55 with a standard deviation of 0.54, in agreement with values reported in [21,50]. It is worth mentioning that the same α is used for all vessels, probably increasing the sensitivity of predicted FFR to this parameter. In fact, it is expected

that tissue located distally to a stenosis, might show a reduced vasodilatory capacity.

The uncertainty about stenosis segmentation, represented by Δr_s in this study, has also shown to play a relevant role in terms of its contribution to overall FFR prediction uncertainty. However, our results show that such role is less relevant for lesions within the critical FFR range between 0.7 and 0.9. Moreover, it must be noted that the range used to model uncertainties in such parameter in this study was rather low. Further assessment of the role of uncertainty in segmented geometries should involve considering such factor over the entire geometry and not only at stenosis locations, by adopting an approach similar to the one reported in [4]. This aspect will be the subject of future work.

It is worth noting that most important parameters in terms of sensitivity and uncertainty of FFR predictions are all ultimately related to the definition of flow through the coronary tree (CO , λ_{cor} and α), which points to the fact that being able to model this variable correctly is of crucial importance for obtaining precise and reliable FFR predictions. Fig. 10 illustrates the achievable reduction in uncertainty if flow could be measured accurately in hyperemia, with particular impact in the critical FFR range between 0.7 and 0.9. Although the velocity of blood in epicardial arteries may be estimated with transthoracic Doppler echocardiography [15], currently such an approach has not been used in the context of model-based FFR prediction, and consequently there is no evidence on whether it can provide useful information or not. In any case, our results show that obtaining accurate estimates for flow is an aspect on which to focus in order to reduce prediction uncertainty and increase accuracy of model-based FFR prediction. Progress in this direction has been reported in [13].

Acknowledgements

This is a pre-print of an article published in *Cardiovascular Engineering and Technology*. The final authenticated version is available online at:
<http://dx.doi.org/10.1007/s13239-018-00388-w>

This work was partially supported by NTNU Health (Strategic Research Area at the Norwegian University of Science and Technology) and by The Liaison Committee for education, research and innovation in Central Norway. Computational resources in Norwegian HPC infrastructure were granted by the Norwegian Research Council by Project Nr. NN9545K.

References

1. Antiga, L., Piccinelli, M., Botti, L., Ene-Iordache, B., Remuzzi, A., Steinman, D.A.: An image-based modeling framework for patient-specific computational hemodynamics. *Medical & Biological Engineering & Computing* **46**(11), 1097–1112 (2008). DOI 10.1007/s11517-008-0420-1. URL <http://link.springer.com/10.1007/s11517-008-0420-1>

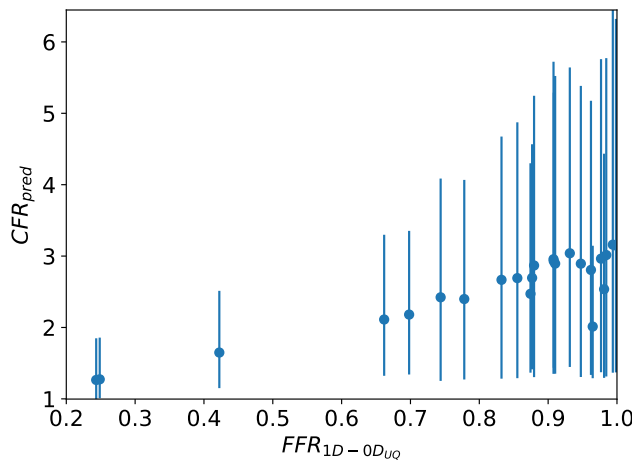


Fig. 11: The mean predicted, CFR versus mean predicted FFR. The error bars represent the 95 % prediction intervals for CFR.

2. Blanco, P.J., Bulant, C.A., Müller, L.O., Talou, G.D.M., Bezerra, C.G., Lemos, P.L., Feijóo, R.A.: Comparison of 1d and 3d Models for the Estimation of Fractional Flow Reserve. arXiv:1805.11472 [physics] (2018). URL <http://arxiv.org/abs/1805.11472>. ArXiv: 1805.11472
3. Boileau, E., Pant, S., Roobottom, C., Sazonov, I., Deng, J., Xie, X., Nithiarasu, P.: Estimating the accuracy of a reduced-order model for the calculation of fractional flow reserve (FFR). International Journal for Numerical Methods in Biomedical Engineering **34**(1), e2908 (2018). DOI 10.1002/cnm.2908. URL <http://doi.wiley.com/10.1002/cnm.2908>
4. Brault, A., Dumas, L., Lucor, D.: Uncertainty quantification of inflow boundary condition and proximal arterial stiffness coupled effect on pulse wave propagation in a vascular network. arXiv preprint arXiv:1606.06556 (2016). URL <http://arxiv.org/abs/1606.06556>
5. Bulant, C., Blanco, P., Maso Talou, G., Bezerra, C.G., Lemos, P., Feijóo, R.: A head-to-head comparison between CT- and IVUS-derived coronary blood flow models. Journal of Biomechanics **51**, 65–76 (2017). DOI 10.1016/j.jbiomech.2016.11.070. URL <http://linkinghub.elsevier.com/retrieve/pii/S002192901631260X>
6. Cook, C.M., Petraco, R., Shun-Shin, M.J., Ahmad, Y., Nijjer, S., Al-Lamee, R., Kikuta, Y., Shiono, Y., Mayet, J., Francis, D.P., Sen, S., Davies, J.E.: Diagnostic Accuracy of Computed Tomography-Derived Fractional Flow Reserve: A Systematic Review. JAMA Cardiology (2017). DOI 10.1001/jamacardio.2017.1314. URL <http://cardiology.jamanetwork.com/article.aspx?doi=10.1001/jamacardio.2017.1314>
7. De Bruyne, B., Pijls, N.H., Kalesan, B., Barbato, E., Tonino, P.A., Piroth, Z., Jagic, N., Möbius-Winkler, S., Rioufol, G., Witt, N., Kala, P., MacCarthy, P., Engström, T., Oldroyd, K.G., Mavromatis, K., Manoharan, G., Verlee, P., Frobert, O., Curzen, N., Johnson, J.B., Jüni, P., Fearon, W.F.: Fractional Flow Reserve–Guided PCI versus Medical Therapy in Stable Coronary Disease. New England Journal of Medicine **367**(11), 991–1001 (2012). DOI 10.1056/NEJMoa1205361. URL <http://www.nejm.org/doi/abs/10.1056/NEJMoa1205361>
8. Dubin, J., Wallerson, D.C., Cody, R.J., Devereux, R.B.: Comparative accuracy of Doppler echocardiographic methods for clinical stroke volume determination. Ameri-

- can Heart Journal **120**(1), 116–123 (1990). DOI 10.1016/0002-8703(90)90168-W. URL <http://www.sciencedirect.com/science/article/pii/000287039090168W>
- 9. Eck, V.G., Donders, W.P., Sturdy, J., Feinberg, J., Delhaas, T., Hellevik, L.R., Huberts, W.: A guide to uncertainty quantification and sensitivity analysis for cardiovascular applications. International Journal for Numerical Methods in Biomedical Engineering pp. n/a–n/a (2015). DOI 10.1002/cnm.2755. URL <http://onlinelibrary.wiley.com/doi/10.1002/cnm.2755/abstract>
 - 10. Eck, V.G., Sturdy, J., Hellevik, L.R.: Effects of arterial wall models and measurement uncertainties on cardiovascular model predictions. Journal of Biomechanics (2016). DOI 10.1016/j.jbiomech.2016.11.042. URL <http://www.sciencedirect.com/science/article/pii/S0021929016312210>
 - 11. Evju, Ø., Alnæs, M.S.: CBCFLOW. Bitbucket repository (2017)
 - 12. Feinberg, J., Langangen, H.P.: Chaospy: An open source tool for designing methods of uncertainty quantification. Journal of Computational Science **11**, 46–57 (2015). DOI 10.1016/j.jocs.2015.08.008
 - 13. Fiorentini, S.: Maximum velocity estimation in coronary arteries using 3d tracking Doppler p. 8
 - 14. Gaur, S., Øvrehus, K.A., Dey, D., Leipsic, J., Bøtker, H.E., Jensen, J.M., Narula, J., Ahmadi, A., Achenbach, S., Ko, B.S., Christiansen, E.H., Kaltoft, A.K., Berman, D.S., Bezerra, H., Lassen, J.F., Nørgaard, B.L.: Coronary plaque quantification and fractional flow reserve by coronary computed tomography angiography identify ischaemia-causing lesions. European Heart Journal **37**(15), 1220–1227 (2016). DOI 10.1093/eurheartj/ehv690. URL <https://academic.oup.com/eurheartj/article-lookup/doi/10.1093/eurheartj/ehv690>
 - 15. Holte, E.: Transthoracic Doppler echocardiography for the detection of coronary artery stenoses and microvascular coronary dysfunction. NTNU (2017). URL <https://brage.bibsys.no/xmlui/handle/11250/2486248>
 - 16. Hunyor, S.N., Flynn, J.M., Cochineas, C.: Comparison of performance of various sphygmomanometers with intra-arterial blood-pressure readings. British Medical Journal **2**(6131), 159–162 (1978). URL <http://www.ncbi.nlm.nih.gov/pmc/articles/PMC1606220/>
 - 17. Huo, Y., Kassab, G.S.: Intraspecific scaling laws of vascular trees. Journal of the Royal Society, Interface **9**(66), 190–200 (2012). DOI 10.1098/rsif.2011.0270. BibTeX[pmid=21676970;pmcid=PMC3223633]
 - 18. Huo, Y., Svendsen, M., Choy, J.S., Zhang, Z.D., Kassab, G.S.: A validated predictive model of coronary fractional flow reserve. Journal of The Royal Society Interface **9**(71), 1325–1338 (2012). DOI 10.1098/rsif.2011.0605. URL <http://rsif.royalsocietypublishing.org/content/9/71/1325>
 - 19. Itu, L., Sharma, P., Mihalef, V., Kamen, A., Suciu, C., Lomaniciu, D.: A patient-specific reduced-order model for coronary circulation. In: 2012 9th IEEE International Symposium on Biomedical Imaging (ISBI), pp. 832–835. IEEE (2012). URL http://ieeexplore.ieee.org/xpls/abs_all.jsp?arnumber=6235677
 - 20. Johnson, N.P., Johnson, D.T., Kirkeeide, R.L., Berry, C., De Bruyne, B., Fearon, W.F., Oldroyd, K.G., Pijls, N.H.J., Gould, K.L.: Repeatability of Fractional Flow Reserve Despite Variations in Systemic and Coronary Hemodynamics. JACC: Cardiovascular Interventions **8**(8), 1018–1027 (2015). DOI 10.1016/j.jcin.2015.01.039. URL <http://www.sciencedirect.com/science/article/pii/S1936879815006998>
 - 21. Johnson, N.P., Kirkeeide, R.L., Gould, K.L.: Is discordance of coronary flow reserve and fractional flow reserve due to methodology or clinically relevant coronary pathophysiology? JACC: Cardiovascular imaging **5**(2), 193–202 (2012). DOI 10.1016/j.jcmg.2011.09.020
 - 22. Jones, E., Oliphant, T., Peterson, P., et al.: SciPy: Open source scientific tools for Python (2001–). URL <http://www.scipy.org/>
 - 23. Kenner, T.: The measurement of blood density and its meaning. Basic Research in Cardiology **84**(2), 111–124 (1989). DOI 10.1007/BF01907921. URL <http://link.springer.com/article/10.1007/BF01907921>
 - 24. Kim, H.J., Vignon-Clementel, I.E., Coogan, J.S., Figueira, C.A., Jansen, K.E., Taylor, C.A.: Patient-Specific Modeling of Blood Flow and Pressure in Human Coronary

- Arteries. *Annals of Biomedical Engineering* **38**(10), 3195–3209 (2010). DOI 10.1007/s10439-010-0083-6. URL <http://link.springer.com/10.1007/s10439-010-0083-6>
- 25. Lewis, J.F., Kuo, L.C., Nelson, J.G., Limacher, M.C., Quinones, M.A.: Pulsed Doppler echocardiographic determination of stroke volume and cardiac output: clinical validation of two new methods using the apical window. *Circulation* **70**(3), 425–431 (1984). Bibtex[pmid=6744546]
 - 26. Liang, F., Fukasaku, K., Liu, H., Takagi, S.: A computational model study of the influence of the anatomy of the circle of willis on cerebral hyperperfusion following carotid artery surgery. *BioMedical Engineering OnLine* **10**, 84 (2011). DOI 10.1186/1475-925X-10-84. URL <https://doi.org/10.1186/1475-925X-10-84>
 - 27. Logg, A., Mardal, K.A., Wells, G. (eds.): Automated Solution of Differential Equations by the Finite Element Method, *Lecture Notes in Computational Science and Engineering*, vol. 84. Springer Berlin Heidelberg, Berlin, Heidelberg (2012). DOI 10.1007/978-3-642-23099-8. URL <http://link.springer.com/10.1007/978-3-642-23099-8>
 - 28. Mantero, S., Pietrabissa, R., Fumero, R.: The coronary bed and its role in the cardiovascular system: a review and an introductory single-branch model. *Journal of Biomedical Engineering* **14**(2), 109–116 (1992). DOI 10.1016/0141-5425(92)90015-D. URL <http://linkinghub.elsevier.com/retrieve/pii/014154259290015D>
 - 29. Matsuda, J., Murai, T., Kanaji, Y., Usui, E., Araki, M., Niida, T., Ichijo, S., Hamaya, R., Lee, T., Yonetsu, T., Isobe, M., Kakuta, T.: Prevalence and Clinical Significance of Discordant Changes in Fractional and Coronary Flow Reserve After Elective Percutaneous Coronary Intervention. *Journal of the American Heart Association* **5**(12) (2016). DOI 10.1161/JAHA.116.004400
 - 30. Morris, P.D., Silva Soto, D.A., Feher, J.F., Rafiroiu, D., Lungu, A., Varma, S., Lawford, P.V., Hose, D.R., Gunn, J.P.: Fast Virtual Fractional Flow Reserve Based Upon Steady-State Computational Fluid Dynamics Analysis. *JACC: Basic to Translational Science* **2**(4), 434–446 (2017). DOI 10.1016/j.jacbs.2017.04.003. URL <http://linkinghub.elsevier.com/retrieve/pii/S2452302X17301353>
 - 31. Mortensen, M., Valen-Sendstad, K.: Oasis: A high-level/high-performance open source Navier-Stokes solver. *Computer Physics Communications* **188**, 177–188 (2015). DOI 10.1016/j.cpc.2014.10.026. URL <http://linkinghub.elsevier.com/retrieve/pii/S0010465514003786>
 - 32. Murray, C.D.: The Physiological Principle of Minimum Work. *Proceedings of the National Academy of Sciences of the United States of America* **12**(3), 207–214 (1926). URL <http://www.ncbi.nlm.nih.gov/pmc/articles/PMC1084489/>
 - 33. Organization, W.H.: Top 10 causes of death (2018). URL <http://www.who.int/news-room/fact-sheets/detail/the-top-10-causes-of-death>
 - 34. Pijls, N.H., Fearon, W.F., Tonino, P.A., Siebert, U., Ikeno, F., Bornschein, B., van't Veer, M., Klauss, V., Manoharan, G., Engstrøm, T., Oldroyd, K.G., Ver Lee, P.N., MacCarthy, P.A., De Bruyne, B.: Fractional Flow Reserve Versus Angiography for Guiding Percutaneous Coronary Intervention in Patients With Multivessel Coronary Artery Disease. *Journal of the American College of Cardiology* **56**(3), 177–184 (2010). DOI 10.1016/j.jacc.2010.04.012. URL <http://linkinghub.elsevier.com/retrieve/pii/S0735109710016025>
 - 35. Ri, K., Kumamaru, K.K., Fujimoto, S., Kawaguchi, Y., Dohi, T., Yamada, S., Takamura, K., Kogure, Y., Yamada, N., Kato, E., Irie, R., Takamura, T., Suzuki, M., Hori, M., Aoki, S., Daida, H.: Noninvasive Computed Tomography – Derived Fractional Flow Reserve Based on Structural and Fluid Analysis: Reproducibility of On-site Determination by Unexperienced Observers. *Journal of Computer Assisted Tomography* p. 1 (2017). DOI 10.1097/RCT.0000000000000679. URL <http://Insights.ovid.com/crossref?an=00004728-90000000-99330>
 - 36. Robert, C.P., Casella, G.: Monte Carlo statistical methods, 2. ed., softcover reprint of the hardcover 2. ed. 2004 edn. Springer texts in statistics. Springer (2010)
 - 37. Rogers, G., Oosthuysse, T.: A Comparison of the Indirect Estimate of Mean Arterial Pressure Calculated by the Conventional Equation and Calculated to Compensate for a Change in Heart Rate. *International Journal of Sports Medicine* **21**(02), 90–95 (2000). DOI 10.1055/s-2000-8865. URL <https://www.thieme-connect.com/products/ejournals/html/10.1055/s-2000-8865?update=true#R616-17>

38. Sakamoto, S., Takahashi, S., Coskun, A.U., Papafakis, M.I., Takahashi, A., Saito, S., Stone, P.H., Feldman, C.L.: Relation of Distribution of Coronary Blood Flow Volume to Coronary Artery Dominance. *The American Journal of Cardiology* **111**(10), 1420–1424 (2013). DOI 10.1016/j.amjcard.2013.01.290. URL <http://linkinghub.elsevier.com/retrieve/pii/S000291491300386X>
39. Saltelli, A.: Making best use of model evaluations to compute sensitivity indices. *Computer Physics Communications* **145**(2), 280–297 (2002). DOI 10.1016/S0010-4655(02)00280-1
40. Saltelli, A.: Global sensitivity analysis : the primer. John Wiley,, Chichester, England (2008). URL <http://catalog.lib.ncsu.edu/record/NCSU2123570>
41. Sankaran, S., Kim, H.J., Choi, G., Taylor, C.A.: Uncertainty quantification in coronary blood flow simulations: Impact of geometry, boundary conditions and blood viscosity. *Journal of Biomechanics* **49**(12), 2540–2547 (2016). DOI 10.1016/j.jbiomech.2016.01.002. URL <http://www.sciencedirect.com/science/article/pii/S0021929016000117>
42. Schroeder, W.J., Martin, K.M.: The Visualization Toolkit. In: *Visualization Handbook*, pp. 593–614. Elsevier (2005). DOI 10.1016/B978-012387582-2/50032-0. URL <http://linkinghub.elsevier.com/retrieve/pii/B9780123875822500320>
43. Shahzad, R., Kirişli, H., Metz, C., Tang, H., Schaap, M., van Vliet, L., Niessen, W., van Walsum, T.: Automatic segmentation, detection and quantification of coronary artery stenoses on CTA. *The International Journal of Cardiovascular Imaging* **29**(8), 1847–1859 (2013). DOI 10.1007/s10554-013-0271-1. BibTeX[pmid=23925713]
44. Simo, J., Armero, F.: Unconditional stability and long-term behavior of transient algorithms for the incompressible Navier-Stokes and Euler equations. *Computer Methods in Applied Mechanics and Engineering* **111**(1-2), 111–154 (1994). DOI 10.1016/0045-7825(94)90042-6. URL <http://linkinghub.elsevier.com/retrieve/pii/0045782594900426>
45. Smith, N., Pullan, A., Hunter, P.: An Anatomically Based Model of Transient Coronary Blood Flow in the Heart. *SIAM Journal on Applied Mathematics* **62**(3), 990–1018 (2002). DOI 10.1137/S0036139999355199. URL <https://epubs.siam.org/doi/abs/10.1137/S0036139999355199>
46. Spaan, J.A.E.: Coronary Blood Flow, *Developments in Cardiovascular Medicine*, vol. 124. Springer Netherlands, Dordrecht (1991). URL <http://link.springer.com/10.1007/978-94-011-3148-3>
47. srl, O.: The Vascular Modeling Toolkit website URL <https://www.vmtk.org>. Accessed: 2017-10-27
48. Sturdy, J., Kjernlie, J.K., Nydal, H.M., Eck, V.G., Hellevik, L.R.: Uncertainty of computational coronary stenosis assessment and model based mitigation of image resolution limitations. Submitted
49. Tonino, P.A., De Bruyne, B., Pijls, N.H., Siebert, U., Ikeno, F., vant Veer, M., Klauss, V., Manoharan, G., Engström, T., Oldroyd, K.G., others: Fractional flow reserve versus angiography for guiding percutaneous coronary intervention. *New England Journal of Medicine* **360**(3), 213–224 (2009). URL <http://www.nejm.org/doi/full/10.1056/NEJMoa0807611>
50. Uren, N.G., Melin, J.A., De Bruyne, B., Wijns, W., Baudhuin, T., Camici, P.G.: Relation between myocardial blood flow and the severity of coronary-artery stenosis. *The New England Journal of Medicine* **330**(25), 1782–1788 (1994). DOI 10.1056/NEJM19940623302503. BibTeX[pmid=8190154]
51. Wongkrajang, P., Chinswangwatanakul, W., Mokkhamakkun, C., Chuangsawanich, N., Wesarachkitti, B., Thaowto, B., Laiwejpithaya, S., Komkhum, O.: Establishment of new complete blood count reference values for healthy Thai adults. *International Journal of Laboratory Hematology* **0**(0). DOI 10.1111/ijlh.12843. URL <https://onlinelibrary.wiley.com/doi/abs/10.1111/ijlh.12843>
52. Xiao, N., Alastrauey, J., Alberto Figueroa, C.: A systematic comparison between 1-D and 3-D hemodynamics in compliant arterial models. *International Journal for Numerical Methods in Biomedical Engineering* **30**(2), 204–231 (2014). DOI 10.1002/cnm.2598. BibTeX[pmid=24115509;pmcid=PMC4337249]
53. Young, D.F., Tsai, F.Y.: Flow characteristics in models of arterial stenoses — I. Steady flow. *Journal of Biomechanics* **6**(4), 395–410 (1973). DOI 10.1016/0021-9290(73)90099-7. URL <http://linkinghub.elsevier.com/retrieve/pii/0021929073900997>

-
54. Yushkevich, P.A., Piven, J., Hazlett, H.C., Smith, R.G., Ho, S., Gee, J.C., Gerig, G.: User-guided 3d active contour segmentation of anatomical structures: Significantly improved efficiency and reliability. *NeuroImage* **31**(3), 1116–1128 (2006). DOI 10.1016/j.neuroimage.2006.01.015. URL <http://linkinghub.elsevier.com/retrieve/pii/S1053811906000632>
 55. Zienkiewicz, O.C., Taylor, R.L., Nithiarasu, P.: The finite element method for fluid dynamics, seventh edition edn. Butterworth-Heinemann, Oxford (2014). OCLC: ocn869413341